

1 **ALICENET - An Italian network of Automated Lidar-Ceilometers** 2 **for 4D aerosol monitoring: infrastructure, data processing, and** 3 **applications**

4 Annachiara Bellini^{1,2,3,*}, Henri Diémoz³, Luca Di Liberto², Gian Paolo Gobbi², Alessandro Bracci⁴,
5 Ferdinando Pasqualini⁴, Francesca Barnaba^{2,*}

6 ¹ University 'La Sapienza', DIET, Rome, Italy

7 ² National Research Council - Institute of Atmospheric Science and Climate, CNR-ISAC, Rome, Italy

8 ³ ARPA Valle d'Aosta, Saint-Christophe, Italy

9 ⁴ National Research Council - Institute of Atmospheric Science and Climate, CNR-ISAC, Bologna, Italy

10 ***Correspondence:** Francesca Barnaba (f.barnaba@isac.cnr.it) and Annachiara Bellini (a.bellini@arpa.vda.it)

11 **Abstract.** Vertically-resolved information on aerosol particles represents a key aspect in many atmospheric studies,
12 including aerosol-climate interactions and aerosol impacts on air quality and human health. This information is primarily
13 derived by lidar active remote sensing, in particular with extensive networks currently in operation worldwide. In Italy, the
14 Institute of Atmospheric Sciences and Climate (ISAC) of the National Research Council (CNR) established a network of
15 Automated Lidar-Ceilometers (ALCs), ALICENET, in 2015. Since then, ALICENET grew up as a cooperative effort of
16 Italian institutions dealing with atmospheric science and monitoring, and currently includes instruments run by regional
17 Environmental Protection Agencies, Universities, Research Centres and private companies. In the current configuration, the
18 network makes use of both single-channel ALCs and dual channel, polarisation-sensitive systems ALCs (referred to as
19 PLCs). The systems operate in very different environments (urban, coastal, mountainous and volcanic areas) from Northern
20 to Southern Italy, thus allowing the continuous monitoring of the aerosol vertical distribution across the country. ALICENET
21 also contributes to the EUMETNET program E-PROFILE, filling an Italian observational gap compared to other EU
22 Member States, these generally running extended ALCs networks through National Meteo Services. In this work, we present
23 the ALICENET infrastructure and the specifically-developed data processing centralised at CNR-ISAC, converting raw
24 instrumental data into quantitative, quality controlled information on aerosol properties, ranging from attenuated backscatter
25 to aerosol mass and vertical stratifications. This setup allows to get insights into the 4D aerosol field over Italy with
26 applications from near real-time monitoring to long-term analyses, examples of which are reported in this work. Specific
27 comparisons of the ALICENET products to independent measurements obtained with different techniques, such as
28 particulate matter (PM) concentrations from in-situ samplers and aerosol optical depth (AOD) from sun photometers, are
29 also included here, revealing the good performances of the ALICENET algorithms. Overall, ALICENET represents a

30 valuable resource to extend the current aerosol observational capabilities in Italy and in the Mediterranean area, and
31 contributes to bridge a gap between atmospheric science and its application to specific sectors, among which air quality,
32 solar energy, aviation safety.

33 1. Introduction

34 Aerosols influence the Earth system and human life in several ways. They affect the planetary radiation budget directly by
35 extinction of solar radiation and indirectly by modification of cloud properties and lifetime, thus also influencing the
36 hydrological cycle (IPCC, 2022). Deteriorating Air Quality (AQ), atmospheric particles of both anthropogenic and natural
37 origin are also a main concern for human health (WHO, 2021). Furthermore, high aerosol loads reduce visibility and, during
38 major events such as desert dust storms, volcanic eruptions, and wide forest fires, can damage aircraft engines, thus
39 representing a threat to the aviation sector (e.g. Flentje et al., 2010; Papagiannopoulos et al., 2020, Brenot et al., 2021;
40 Monteiro et al., 2022, Ryder et al., 2024). The vertical aerosol distribution is a key aspect to correctly quantify aerosol
41 effects on climate and human activities, this being related to radiative transfer and atmospheric heating rates (e.g., Fasano et
42 al., 2021; Fountoulakis et al. 2022), aerosol-cloud-precipitation interactions (e.g., Napoli et al., 2022), particle dispersion and
43 transformation processes (e.g., Curci et al., 2015; Gobbi et al., 2019; Diémoz et al., 2019a,b), the state of high-altitude,
44 pristine environments (e.g., Balestrini et al., 2024).

45 Active remote sensing through lidar sensors is a very efficient tool to provide range-resolved, accurate profiles of aerosol
46 properties (e.g., Gobbi et al., 2001; Tesche et al. 2009; Ansmann et al., 2011). In the last decades, both ground-based and
47 space-based lidar systems have been developed and widely used for scientific research purposes, and they are expected to
48 play an increasingly important role in climate and public health studies (Remer et al., 2024). From space, the recently
49 dismissed NASA-CNES CALIOP sensor onboard CALIPSO (Winker et al., 2010) provided one of the most valuable,
50 vertically-resolved, global aerosol datasets (2006-2023), that is expected to be extended by the just launched ESA-JAXA
51 mission EarthCARE (Cloud, Aerosol and Radiation Explorer, Illingworth et al., 2015). From the ground, lidar remote
52 sensing is often performed in the framework of globally distributed research networks. In Europe, a wide Aerosol Research
53 Lidar Network (EARLINET, Pappalardo et al., 2010) has been developed in the last decade, which is currently an important
54 component of the European Strategy Forum on Research Infrastructures - Aerosol, Clouds, and Trace Gases Research
55 Infrastructure (ESFRI - ACTRIS). Such a research-oriented network runs high power, multi-wavelength Raman lidar
56 systems, which were not designed for monitoring purposes. In fact, EARLINET lidar measurements are generally not
57 performed continuously, and the spatial density of the measuring sites is still insufficient to capture the high spatio-temporal
58 variability characterising aerosols.

59 In the last two decades, the use of automatic, low-energy, affordable and robust single-channel elastic lidars, referred to as
60 Automated Lidar-Ceilometers (ALCs), spread out. These systems emit single-wavelength laser pulses, mostly in the infrared
61 range, and measure the time- (thus range-) dependent radiation that is elastically backscattered by atmospheric components
62 (molecules, aerosols, cloud droplets/ice crystals). ALCs were originally conceived to only monitor the ‘cloud ceiling’, but

63 recent technological improvements enabled ALCs to provide continuous information on aerosol profiles within the
64 troposphere, including the boundary layer region, albeit with a lower Signal-to-Noise Ratio (SNR) compared to high-power
65 research lidars. This favoured the development of extended networks of such systems worldwide, among which the NASA
66 Micro-Pulse Lidar Network (MPLnet; Welton et al., 2018), the US Environmental Protection Agency (EPA) network for
67 Photochemical Assessment Monitoring Stations (PAMS; Caicedo et al., 2020), or the Asian Dust and aerosol lidar
68 observation network (ADnet; Shimizu et al., 2016). In Europe, several Member States currently run dense ALC networks for
69 monitoring purposes, mostly managed by national meteorological services, such as the DWD in Germany (Flentje et al.,
70 2021) and the MetOffice in the UK (Osborne et al., 2022). Recently, ACTRIS started considering automatic low-power
71 lidars as useful tools within its Aerosol Remote Sensing (ARS) component, although these systems are not yet included in
72 the relevant ‘minimum’ or ‘optimal’ setups recommended by ACTRIS-ARS
73 (<https://www.actris.eu/topical-centre/cars/announcements-resources/documents>, last access: 25-07-2024). Most ALC
74 observations at EU level are currently collected and further exploited in the framework of the E-PROFILE program run by
75 the European Meteorological Services Network EUMETNET
76 (<http://www.eumetnet.eu/activities/observations-programme/current-activities/e-profile/>, last access: 25-07-2024). The
77 development of such an extended ALC observational capacity was further accelerated after the eruption of the Icelandic
78 volcano Eyjafjallajökull in 2010, which disrupted air transport due to the lack of readily accessible information on the
79 horizontal and vertical displacement of the aerosol plume (Flentje et al., 2010, Mortier et al., 2013). Moreover, ALCs have
80 been proven to be extremely useful in support of AQ evaluations, providing information on the vertical dilution of pollutants,
81 transboundary transport of particles from medium-to-long-range distances (e.g., Rizza et al., 2017; Bucci et al., 2018;
82 Diémoz et al., 2019a,b), secondary aerosol formation (e.g., Curci et al., 2015), or even particles reaching the boundary layer
83 through evaporating rain (virgas, e.g., Karle et al., 2023). However, with few exceptions, standard Air Quality Monitoring
84 Networks (AQMNs) in the EU currently miss such profiling capability. The feasibility of filling this gap is currently
85 explored in the framework of the EC-H2020 Project RI-URBANS (<https://riurbans.eu>, last access: 25-07-2024), aiming at
86 the development of service tools in support to AQ monitoring in European urban areas and pollution hotspots. In fact, the
87 current ALC technology has been proven to be mature enough to allow a robust retrieval of the planetary boundary layer
88 height (Kotthaus et al., 2023), a key parameter in AQ, and evaluations are currently ongoing at the EU level to assess
89 readiness of ALC-based retrievals for quantitative Particulate Matter (PM) monitoring (e.g., Shang et al., 2021; Osborne et
90 al., 2024). The recently completed EC Action PROBE (PROfiling the atmospheric Boundary layer at European scale; Cimini
91 et al., 2020; Kotthaus and Bravo Aranda, 2024) supported by the European Cooperation in Science and Technology (COST)
92 was key to promote and coordinate such activities, which are now further explored within the E-PROFILE and ACTRIS
93 communities.

94 In Italy, an effort to coordinate ALC activities at national level and contribute to E-PROFILE has been done by the National
95 Research Council - Institute of Atmospheric Sciences and Climate (CNR-ISAC), which set up the ALICENET network in
96 2015 (<https://www.alice-net.eu/>, last access: 25-07-2024), filling an observational gap over Italy.

97 The ALICENET measurements are particularly relevant in for Mediterranean area, this being a climatic hotspot (IPCC,
98 2022) affected by a complex mixture of atmospheric circulations (e.g., Lelieveld et al., 2002) and aerosol types (e.g.,
99 Barnaba and Gobbi, 2004; Di Iorio et al., 2009; Andres Hernandez et al., 2022). ALICENET is conceived as an open
100 consortium with increasing contributions from several collaborating Partners, among which regional Environmental
101 Protection Agencies, Universities, Research Institutions, and private companies.

102 The present work aims at presenting the ALICENET infrastructure and its data processing chain, designed to derive
103 quantitative and quality checked vertically-resolved information on aerosol properties and layering. The ALICENET data
104 processing, centralised at CNR-ISAC, allows the homogeneous retrieval of aerosol properties from North to South Italy. It is
105 based on specifically developed algorithms, taking benefit from past and ongoing collaborations with the EU ALC-
106 community, particularly in the framework of the EC COST Actions TOPROF (2013-2016) and PROBE (2019-2024), the
107 H2020 Project RI-URBANS (2021-2015), and the E-PROFILE initiative (2019-2023, 2024-2028).

108 The work is organised as follows. Section 2 describes the ALICENET infrastructure. Section 3 introduces the main data
109 processing steps and includes different examples of the relevant ALICENET products and accuracy. To facilitate the
110 reading, the detailed technical aspects of each processing step were included in separated supplement sections (S1-S6), these
111 being thus targeted to readers interested in a deep understanding of the processing chain, and possibly in reproducing it. Sect.
112 4 shows three examples of the near-real time ALICENET monitoring capability, while Sect. 5 summarises the ALICENET
113 achievements and some foreseen future developments within the network.

114 2. ALICENET sites and instruments

115 The ALICENET stations are geographically distributed from the North to the South of the Italian peninsula as shown in Fig.
116 1. The network configuration allows the monitoring of aerosol vertical profiles over a wide range of environmental and
117 atmospheric conditions (e.g. urban, coastal and mountain) within the Mediterranean area. In fact, some stations are located in
118 highly anthropised areas, such as those in the Po Valley and main urban/industrial sites in Italy (Milan, Genova, Turin,
119 Florence, Rome, Taranto), some operate in coastal sites (e.g. Genova, Taranto, Lamezia Terme, Messina, Capo Granitola,
120 Catania), and other at high-altitude (> 550 m asl) stations (Aosta, Mt Cimone, Potenza, Mt. Etna). Most sites are frequently
121 impacted by desert dust advections, particularly relevant in Central and Southern Italy (e.g. Barnaba et al., 2017; Gobbi et
122 al., 2019; Barnaba et al., 2022), and by both short- and long-range transport of biomass burning plumes (e.g. Barnaba et al.,
123 2011). Volcanic plumes are also registered in the ALICENET southernmost sites, mainly in the 5 stations located at the
124 foothills of the Etna volcano, and in the Messina and Lamezia Terme stations, due to their proximity to the other active
125 sicilian volcano of Stromboli.



126

127 **Figure 1:** Location and naming of the ALICENET stations (panel a, bullets). The yellow rectangle over Sicily in panel a) is zoomed in
 128 panel b) to show location of the 5 stations in the Etna volcano area, from the northern to the southern foothills, down to the city of Catania.

129 Background Map credits: a) EUMETSAT, and b) Google Maps.

130

131 For homogeneity of operations, since the beginning of the ALICENET activities (set as 1st January 2016), it was agreed to
132 operate standardised systems across the network choosing the ones that allow to probe at least up to the middle troposphere,
133 also for calibration purposes (e.g., Wiegner et al., 2014; see also Sect. 3.2). The single-channel, bistatic CHM15k
134 instruments manufactured by Lufft (formerly Jenoptik ESW and now Ott Hydromet) were selected for this purpose. These
135 are bi-static ALCs with a Nd:YAG solid-state laser emitting linearly polarised light at 1064 nm, with a 5-7 kHz repetition
136 rate, a maximum vertical resolution of 5 m and a maximum range of 15 km. The only exception in this instrumental setup
137 was a modified-CHM15K prototype with polarisation-sensitive capabilities designed and developed in 2013 by Jenoptik
138 ESW in collaboration with CNR-ISAC in the framework of the EC Life+ DIAPASON project (Gobbi et al., 2019). This first
139 ever polarisation-sensitive ALC (hereafter PLC) was conceived to explore the possibility of producing an affordable, robust
140 system to be widely used in the identification and profiling of non-spherical (e.g. mineral dust) aerosol layers. The prototype
141 PLC was tested in Rome (Italy), where it has been operating successfully since then (e.g., Gobbi et al., 2019; Andres
142 Hernandez et al., 2022), but was never marketed by Lufft. More recently, PLC systems have been made available on the
143 market by Vaisala (CL61 systems, operating at 910 nm) and, due to the important capability of such instruments to
144 discriminate particle sphericity/non sphericity, these are being progressively included in ALICENET.

145 For both CHM15k ALCs and CL61 PLCs, the signal is characterised by high temporal and vertical resolution, with some
146 variability depending on the system type and configuration (e.g., in ALICENET the CHM15k standard configuration implies
147 a vertical and temporal resolutions of 15 m and 15 s, respectively). A summary table with details on the ALICENET sites
148 and instrumentation operating therein is provided in Table 1. It includes indication of the beginning of operations in each site
149 of the ALICENET network (joining date), or the operating period for those systems no longer active. Some systems joined
150 the network very recently and are thus indicated as ‘ready to go’ as instrumental set up and data transfer to the ALICENET
151 database is currently in progress.

152

Name	Lat	Lon	Altitude (m a.s.l.)	System Type	Status	Joining Date or Operating period	Reference Institution (Collaborating Institution)
Aosta 1	45° 44' 32"N	07° 21' 24"E	555	ALC (Lufft CHM15k)	active	02/05/2015	Arpa Valle d'Aosta (CNR-ISAC)
Aosta 2	45° 44' 32"N	07° 21' 24"E	555	PLC (Vaisala CL61)	active	28/07/2023	Arpa Valle d'Aosta (CNR-ISAC)
Milano Bicocca	45° 30' 38"N	09° 12' 42"E	135	ALC (Lufft CHM15k)	active	01/01/2016	CNR-ISAC (Univ. Milano Bicocca)
Milano Rubattino	45° 28' 38"N	09° 15' 41"E	110	PLC (Vaisala CL61)	active	31/05/2023	RSE (CNR-ISAC)
Torino	45° 03' 28"N	07° 39' 24"E	250	PLC (Vaisala CL61)	active	20/06/2023	Politecnico Torino (CNR-ISAC)
San Pietro Capofiume	44° 39' 12"N	11° 37' 24"E	135	ALC (Lufft CHM15k)	ended	13/12/2011 – 17/01/2015	CNR-ISAC
Genova	44° 24' 41"N	08° 53' 30"E	10	PLC (Vaisala CL61)	active	04/12/2022	Arpa Liguria (CNR-ISAC)
Monte Cimone	44° 11' 35"N	10° 42' 05"E	2165	ALC (Lufft CHM15k)	active	13/06/2022	CNR-ISAC
Firenze	43° 49' 08"N	11° 12' 06"E	60	PLC (Vaisala CL61)	ready to go		CNR-IBE (CNR-ISAC)
Roma Down Town	41° 54' 34"N	12° 29' 48"E	58	PLC (Lufft Prototype)	active	13/05/2015	CNR-ISAC (Arpa Lazio)
Castel di Guido	41° 53' 22"N	12° 15' 59"E	135	ALC (Lufft CHM15k)	ended	10/09/2013 – 18/12/2014	CNR-ISAC
Roma Tor Vergata	41° 50' 32"N	12° 38' 50"E	100	ALC (Lufft CHM15k)	active	01/01/2016	CNR-ISAC
Potenza	40° 36' 50"N	15° 43' 26"E	760	ALC (Lufft CHM15k)	active	21/03/2024	CNR-IMAA (CNR-ISAC)
Taranto	40° 29' 37"N	17° 13' 01"E	17	ALC (Lufft CHM15k)	active	01/01/2014	Arpa Puglia (CNR-ISAC)
Lamezia Terme	38° 52' 35"N	16° 13' 56"E	5	ALC (Lufft CHM15k)	active	29/11/2023	CNR-ISAC
Messina	38° 11' 41"N	15° 34' 22"E	5	ALC (Lufft CHM15k)	active	22/06/2016	CNR-ISAC (CNR-IRBIM)
Etna Acireale	37° 38' 26"N	15° 10' 55"E	12	ALC (Lufft CHM15k)	ready to go		Etna High Tech (INGV, CNR-ISAC)
Etna Piedimonte Etneo	37° 47' 31"N	15° 08' 18"E	720	ALC (Lufft CHM15k)	ready to go		INGV (Etna High Tech, CNR-ISAC)
Etna Nicolosi	37° 36' 49"N	15° 01' 11"E	730	PLC (Vaisala CL61)	active	15/03/2023	INGV (Etna High Tech CNR-ISAC)
Etna San Giovanni La Punta	37° 34' 44"N	15° 06' 11"E	350	ALC (Lufft CHM15k)	active	08/06/2022	Etna High Tech (INGV, CNR-ISAC)
Capo Granitola	37° 34' 16"N	12° 39' 35"E	5	ALC (Lufft CHM15k)	active	19/05/2021	CNR-ISAC
Catania Airport Fontanarossa	37° 27' 59"N	15° 04' 57"E	10	ALC (Lufft CHM15k)	ready to go		SAC (Etna High Tech, INGV, CNR-ISAC)

Table 1: ALICENET sites from northern to southern Italy, and relevant details.

154

155

156

13

14

157 3. ALICENET data processing and relevant products

158 The ALICENET data processing chain is summarised in Fig. 2, with indication of main inputs and outputs. It starts with
159 generation of standardised and harmonised data files from instrumental raw data (using the raw2l1 tool,
160 <https://gitlab.in2p3.fr/ipsl/sirta/raw2l1>, last access: 25-07-2024), and then proceeds with pre-processing and calibration
161 procedures, the inversion of the ALC signal into aerosol properties, and the detection of aerosol layers. It is convenient to
162 first introduce the main equations and variables used in the description of the different steps.

163 As in any elastic backscatter lidar, the raw signal $P(r,t)$ recorded by the ALC is a function of the distance from the emitter
164 (range, r) and of the observation time t , and can be described through the lidar equation:

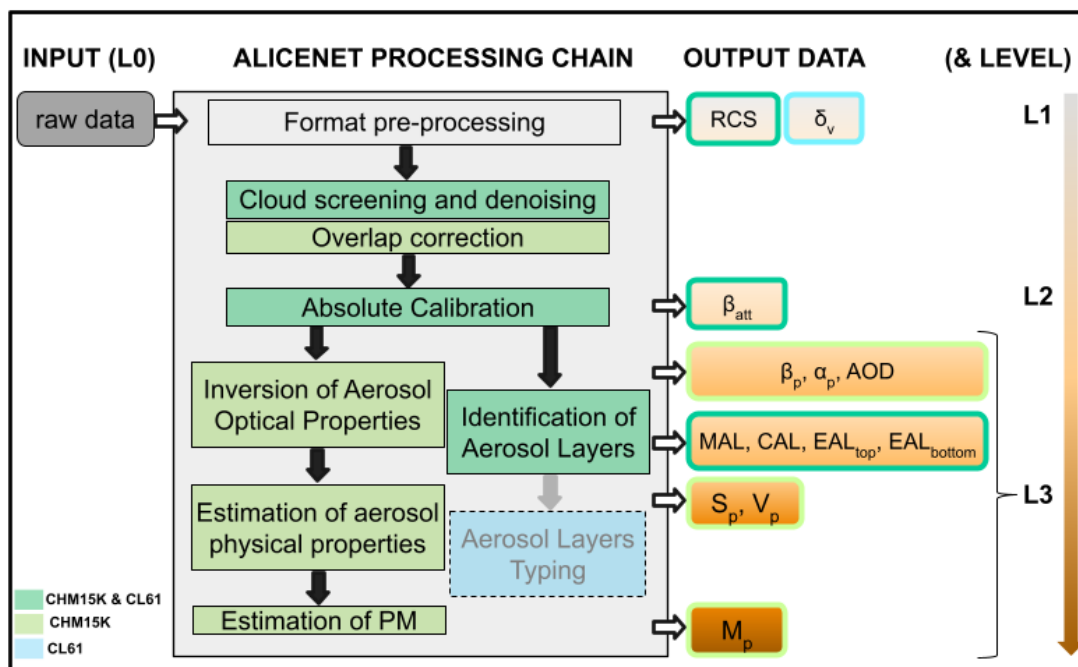
$$165 \quad P(r,t) = r^{-2} \text{Ovl} C_L (\beta_p(r,t) + \beta_m(r,t)) e^{-2 \int_0^r (\alpha_p(r',t) + \alpha_m(r',t)) dr'} \quad (1)$$

166 Equation 1 includes the particle (p) and molecule (m) backscatter (β) and extinction (α) coefficients at the laser wavelength,
167 and some instrumental factors, embedded into the instrument-specific calibration coefficient C_L . Furthermore, particularly
168 for bistatic systems (i.e., the CHM15k), measurements in the near range (generally < 500-700 m) are affected by signal
169 losses due to the incomplete superposition (overlap) of the laser beam and the receiver field of view. The term Ovl in Eq. 1
170 therefore indicates the instrument-specific overlap function used to correct the signal loss in the near range. Equation 1
171 allows to simply derive the total (i.e., aerosol + molecules) attenuated backscatter, β_{att} , as follows:

$$172 \quad \beta_{att}(r,t) = \frac{P(r,t)r^2}{\text{Ovl}(r,t)C_L(t)} = (\beta_p(r,t) + \beta_m(r,t)) e^{-2 \int_0^r (\alpha_p(r',t) + \alpha_m(r',t)) dr'} \quad (2)$$

173
174 The complete ALICENET data processing chain (Fig. 2) includes pre-processing procedures (namely cloud screening,
175 denoising, and overlap correction; Sect. 3.1), the absolute calibration (to determine C_L and, in turn, β_{att} ; Sect. 3.2), the
176 quantitative retrieval of aerosol optical (β_p and α_p) and physical (surface area, S_p , volume, V_p , and mass concentrations, M_p or
177 PM) properties (Sect. 3.3) using an ALICENET-original approach, and the detection of aerosol layers (Mixed, Continuous,
178 and Elevated Aerosol Layers, MAL, CAL, and EALs, respectively) through the ALICENET automatic Aerosol LAYer
179 DetectIoN algorithm (ALADIN; Sect. 3.4). The full processing chain is currently applied to CHM15k systems since, as
180 mentioned above, these were the ones firstly implemented in the network. A similar scheme is under development for CL61
181 systems, for which data processing is currently limited to the cloud screening and denoising, the absolute calibration to
182 monitor the stability of the instrument, and the detection of aerosol layers.

183



185 **Figure 2:** Scheme of the ALICENET processing chain from the raw (L0) data to aerosol products (L1-L3). The different colours in the
 186 processing box are used to indicate inversion steps valid for CHM15k (light green), CL61 (cyan), or both (dark green) systems. This same
 187 colour code (bounding box) is used for relevant output data products, which are further coloured from light to dark orange indicating
 188 processing level, from the more basic L1 quantities (Range-Corrected Signal, RCS, and depolarisation, δ_v , profiles), through the L2 total
 189 attenuated backscatter (β_{att}) to the L3 aerosol optical (particle backscatter, β_p , and extinction, α_p) and physical (particle surface area, S_p ,
 190 volume, V_p , and mass concentrations, M_p or PM) properties and layers (Mixed, Continuous, and Elevated Aerosol Layers, MAL, CAL, and
 191 EALs, respectively).

192
 193 The ALICENET processing chain is completely automatic and allows continuous monitoring of the aerosol field over Italy,
 194 with L1/L2 data visualisation accessible in near-real time through a dedicated website (<https://www.alice-net.eu/>, last access:
 195 25-07-2024). Selected examples of this monitoring capability are provided in Sect. 4. The more advanced, quantitative
 196 retrieval of aerosol properties and layering (L3 products) is currently performed in post-processing and is planned to be
 197 released in the future through the ALICENET website.

198
 199

200 3.1 Pre-processing

201 After the input data format harmonisation, the first pre-processing steps are aimed at avoiding cloud, precipitation, and noise
202 contamination in aerosol retrievals (Sect. 3.1.1). Then data need to be corrected for overlap artefacts (Sect. 3.1.2) before
203 proceeding with the determination of the instrument-specific calibration coefficient (Sect. 3.2). The way these preliminary
204 steps are performed within ALICENET is described hereafter.

205 3.1.1 Cloud-screening and denoising

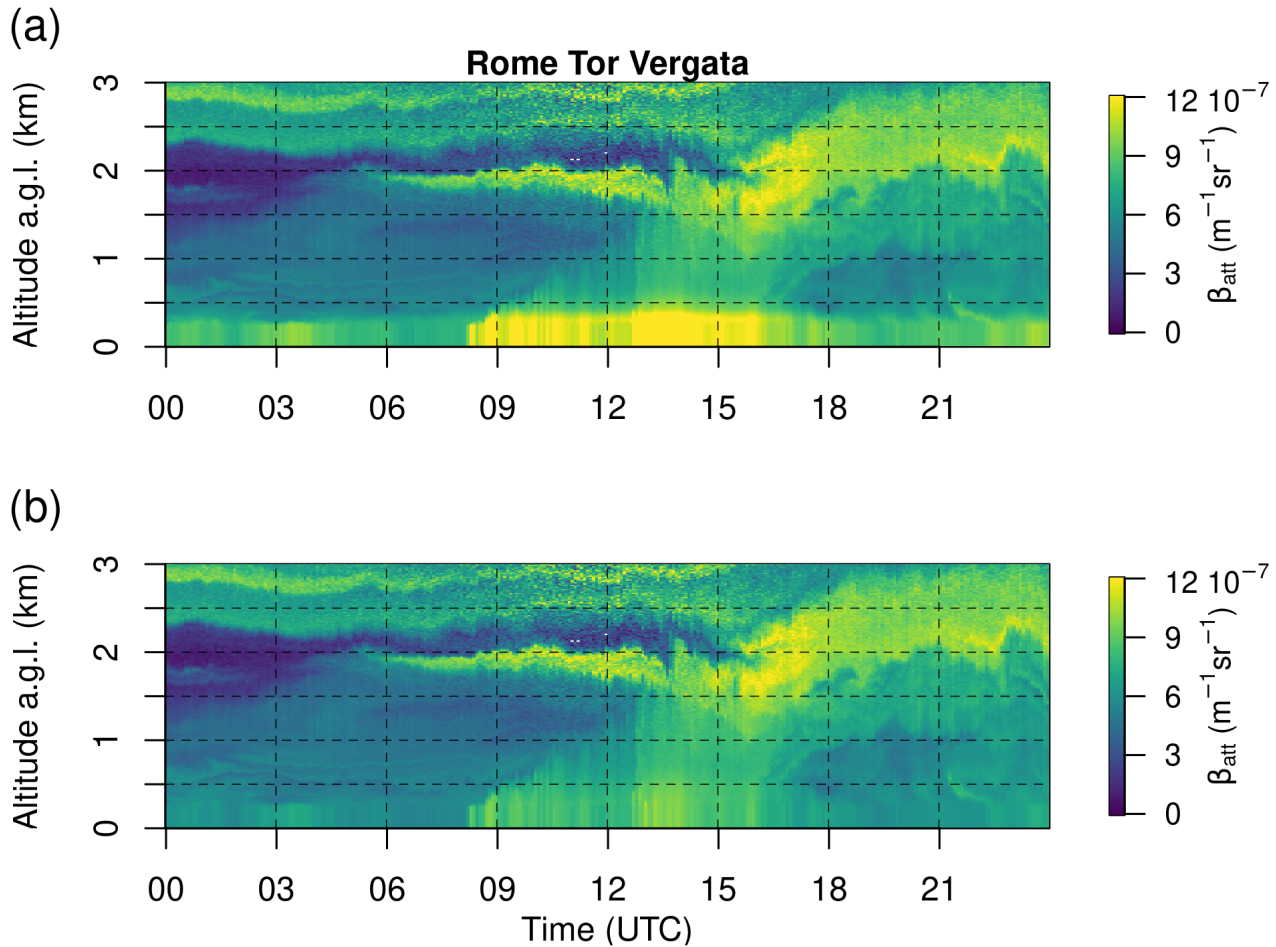
206 At the ALC laser wavelengths clouds generally produce complete extinction of the laser beam above the cloud base. Only in
207 case of optically thin clouds the laser beam is partially transmitted above the cloud base, although in most cases the return
208 signal has a too low SNR to be employed for aerosol retrievals. The cloud-screening applied to the ALICENET data exploits
209 the cloud base height identified by the ALC firmware, with additional requirements to avoid the presence of cloud droplets
210 frequently observed below the cloud base. Technical details of this procedure are reported in supplement S1.

211 Cloud-screened profiles are then downscaled and denoised to improve accuracy of the aerosol retrievals. Indeed, as
212 mentioned above, the ALC signal is generally collected with high temporal and vertical resolution and features a decrease of
213 the SNR along the profile. Denoising is performed by computing signal mean and standard deviation over specific time and
214 range windows, and filtering those data where the SNR (defined as the ratio between the mean and the standard deviation) is
215 below a given threshold. A minimum SNR of 20% is generally set for aerosol retrievals within ALICENET. The temporal
216 resolution of the downscaled data is tuned depending on the time scales of the processes to be investigated. It may range
217 from 1 min for the investigation of boundary layer dynamics up to 3 hours for the identification of aerosol loaded/aerosol
218 free regions in the upper troposphere, such as within the absolute calibration procedure.

219 3.1.2 Overlap correction

220 For bistatic systems such as CHM15k, an overlap correction of the signal in the near range is required (see Eq. 1). This is
221 particularly important when ALC data are used for surface AQ applications, and especially in those conditions in which
222 particulate matter is confined in the lowermost atmospheric levels. An instrument-specific overlap function accounting for
223 signal losses is generally provided by the manufacturer ($Ov_{l_{man}}(r)$). However, it has been demonstrated that changes in the
224 instrument sensitivity rather require the use of an instrument-specific, temperature-dependent overlap correction. Within
225 ALICENET, the derivation of such an overlap correction is largely based on the procedure developed by Hervo et al. (2016).
226 Full details on its implementation in ALICENET including additional quality control and quality assurance criteria
227 (QC/QA.OVL) added to the Hervo et al. (2016) procedure are described in supplement S2. The result is an instrument-,
228 range- and temperature-dependent 'overlap model' $Ov_{l_{model}}(r,T)$ to be used in Eq. 1.

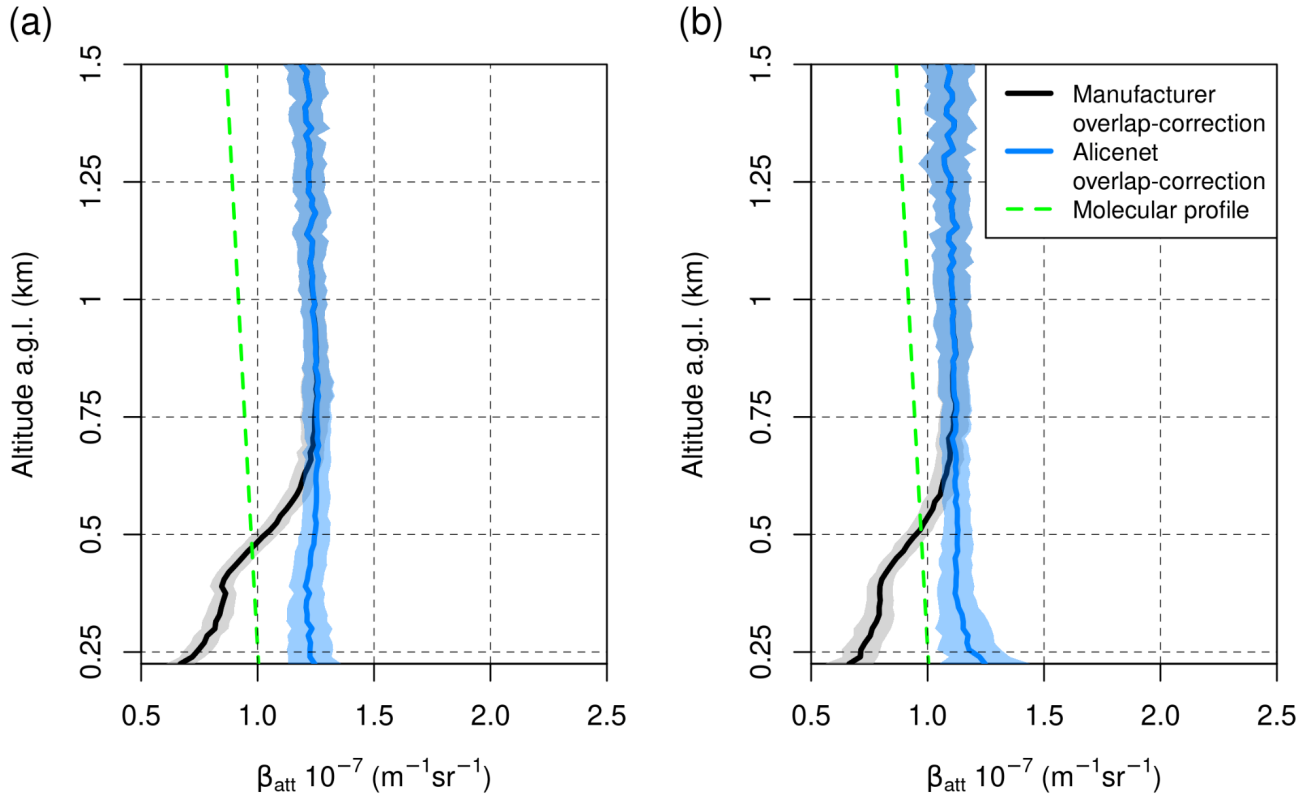
229 Figure 3 shows an example of application of the overlap model on ALC data collected in Rome-Tor Vergata on 12 August
 230 2019. This date was selected because of the high diurnal variation (15 K) of the instrument internal temperature. In Fig. 3,
 231 the continuous (24h) β_{att} profiles derived using both the manufacturer overlap function (panel a) and the ALICENET overlap
 232 model (panel b) are shown. It is evident that the temperature-dependent overlap model is effective in correcting the false-
 233 gradient and the aerosol overestimation in the lowermost 500 m coming from the manufacturer function.
 234



236 **Figure 3:** Overlap-corrected ALC profiles using: (a) the manufacturer overlap function, and (b) the ALICENET overlap correction. Data
 237 refer to the ALICENET Rome-Tor Vergata site on 12/08/2019.
 238

239 A further effort to evaluate the ability of this overlap correction procedure to provide reliable results was conducted in the
240 ALICENET mountain site of Aosta, by exploiting the clean, nearly-molecular conditions often registered at this alpine
241 station. In fact, due to its location, Aosta is frequently characterised by relatively low aerosol concentrations in the
242 lowermost levels, in particular during Föhn events (e.g., Mira-Salama et al., 2008). This makes it possible to compare the
243 overlap-corrected β_{att} profiles with a theoretical molecular profile at very low altitudes. To perform this exercise, Föhn-
244 related, aerosol-free conditions of 3-to-6 hours were identified by exploiting multi-sensor aerosol datasets (namely, surface
245 PM_{10} concentrations measured by an Optical Particle Counter, OPC, and sun photometer-derived Aerosol Optical Depth,
246 AOD) and meteorological parameters (wind, pressure, Relative Humidity) from the AQMN of ARPA Valle d'Aosta
247 (Diémoz et al., 2021). For each of these selected cases, the mean β_{att} profiles retrieved using both the manufacturer and the
248 ALICENET overlap correction were compared with a theoretical molecular profile. Figure 4 shows results for two cases
249 (referring to 25 May 2021 and 6 October 2021) characterised by different values of the instrument internal temperature (308
250 K and 292 K, respectively) and very low aerosol loads both at the surface ($\text{PM}_{10} < 6$ and $5 \mu\text{g m}^{-3}$, respectively) and along the
251 atmospheric column (AOD at 1020 nm < 0.04 and 0.03 , respectively).

252



254 **Figure 4:** β_{att} profiles at 1064 nm derived using the manufacturer overlap function (black line) and the ALICENET overlap correction
 255 (blue line) in two nearly-molecular conditions registered in Aosta on: (a) 25 May 2021 (5-8 UTC), and (b) 6 October 2021 (9-12 UTC).
 256 The shaded areas represent the β_{att} standard deviations within the selected time windows. A reference, molecular-only β_{att} profile is also
 257 reported (green line).

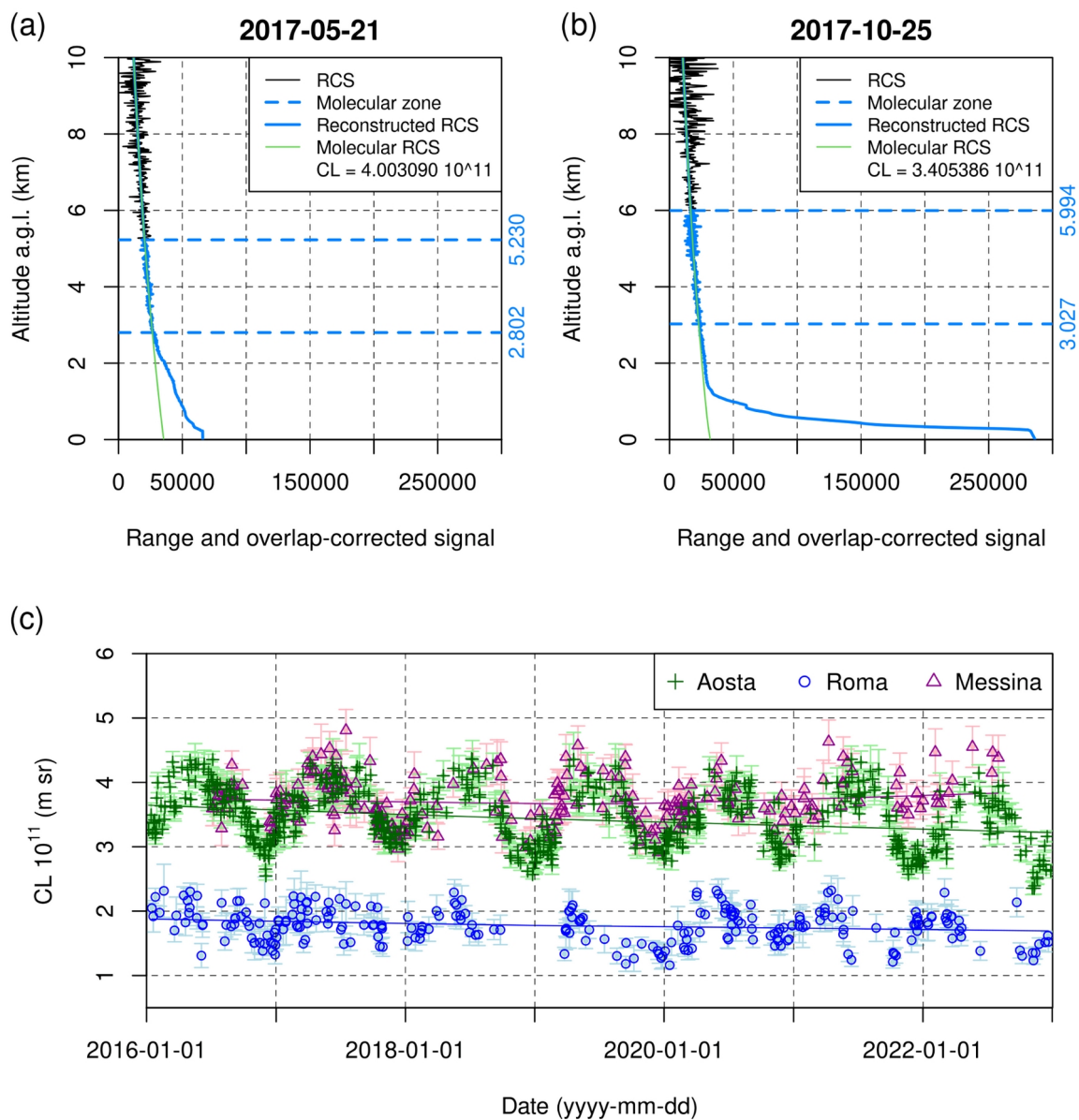
258
 259 Overall, the results show that, while the manufacturer overlap function is unable to properly account for signal losses and
 260 leads to unphysical values lower than the molecular profile in the firsts 750 m, the β_{att} profiles retrieved using the
 261 ALICENET overlap correction reasonably approach the nearly-homogeneous, nearly-molecular theoretical profiles expected
 262 in the selected episodes down to the ground.

263 3.2 Absolute calibration

264 Aim of the absolute calibration is the derivation of the calibration coefficient C_L (see Eq. 1), which is required to convert the
265 ALC signal into quantitative aerosol information. The ALICENET calibration procedure is based on the comparison of the
266 pre-processed ALC signal with a theoretical molecular profile in aerosol-free atmospheric regions (Rayleigh calibration;
267 Klett, 1985), typically in the middle troposphere. The procedure, which is fully automatic, is made in two steps: a) search
268 for the best-suitable molecular window, and b) computation of the calibration coefficient. It was built on the E-PROFILE
269 algorithm, although some specificities and quality controls (QC.CAL) were introduced in both steps. Full description of the
270 technical implementation of these steps is given in the supplement S3.

271 Hereafter, we show two examples of successful calibrations (Fig. 5a, b) and the multi-annual record of C_L (Fig. 5c) derived
272 from three ALICENET systems in northern, central, and southern Italy (Aosta, Roma, and Messina, respectively). Figures 5a
273 and 5b refer to the ALICENET calibrations of the CHM15k in Aosta on 21 May and 25 October 2017, selected as these
274 spring and autumn nighttime calibrations correspond to C_L close to the maximum and minimum values over the year 2017
275 (see Fig. 5c). Figure 5c gives a more general overview of the long-term results of the calibration procedure, further revealing
276 that the three C_L time series feature a similar seasonal cycle, as also observed in other European ALC networks (e.g.,
277 Buxmann, 2024). The reasons for such a yearly cycle are currently under investigation within the European ALC
278 community, also taking advantage of recent activities conducted within the EC COST Action PROBE (e.g., Van Hove and
279 Diémoz, 2024).

280
281
282
283
284
285
286
287
288



290 **Figure 5:** (a, b) Examples of application of the ALICENET calibration procedure, referring to the nighttime range-corrected signals from
 291 the Aosta CHM15k on 21 May and 25 October 2017, with indication of the selected molecular windows and derived calibration
 292 coefficients (C_L). (c) Multi-annual (2016-2022) time series of C_L derived for the CHM15k systems operating in Aosta, Rome, and
 293 Messina, and associated Loess fits (lines) used to derive the C_L values used in the operational, all-year-round data inversions.

294

295 The C_L values used within ALICENET inversions are currently obtained by filtering out the seasonal cycle and keeping only
296 the long-term trends related to slow instrument changes (details are given in supplement S3). Once the main driver of the C_L
297 seasonality will be better identified, it will be taken into account in the calibration procedure. For now, we prefer to use the
298 described approach and estimate the uncertainty associated with this C_L variability (see Sect. 3.3.3).

299 3.3 Retrieval of aerosol properties

300 This section describes the ALICENET inversion of the aerosol optical (Sect. 3.3.1) and physical (Sect. 3.3.2) properties.
301 Specific examples of the aerosol products at different ALICENET sites are also given and compared to a series of
302 independent datasets in order to evaluate the relevant retrieval procedure performances.

303 3.3.1 Aerosol optical properties

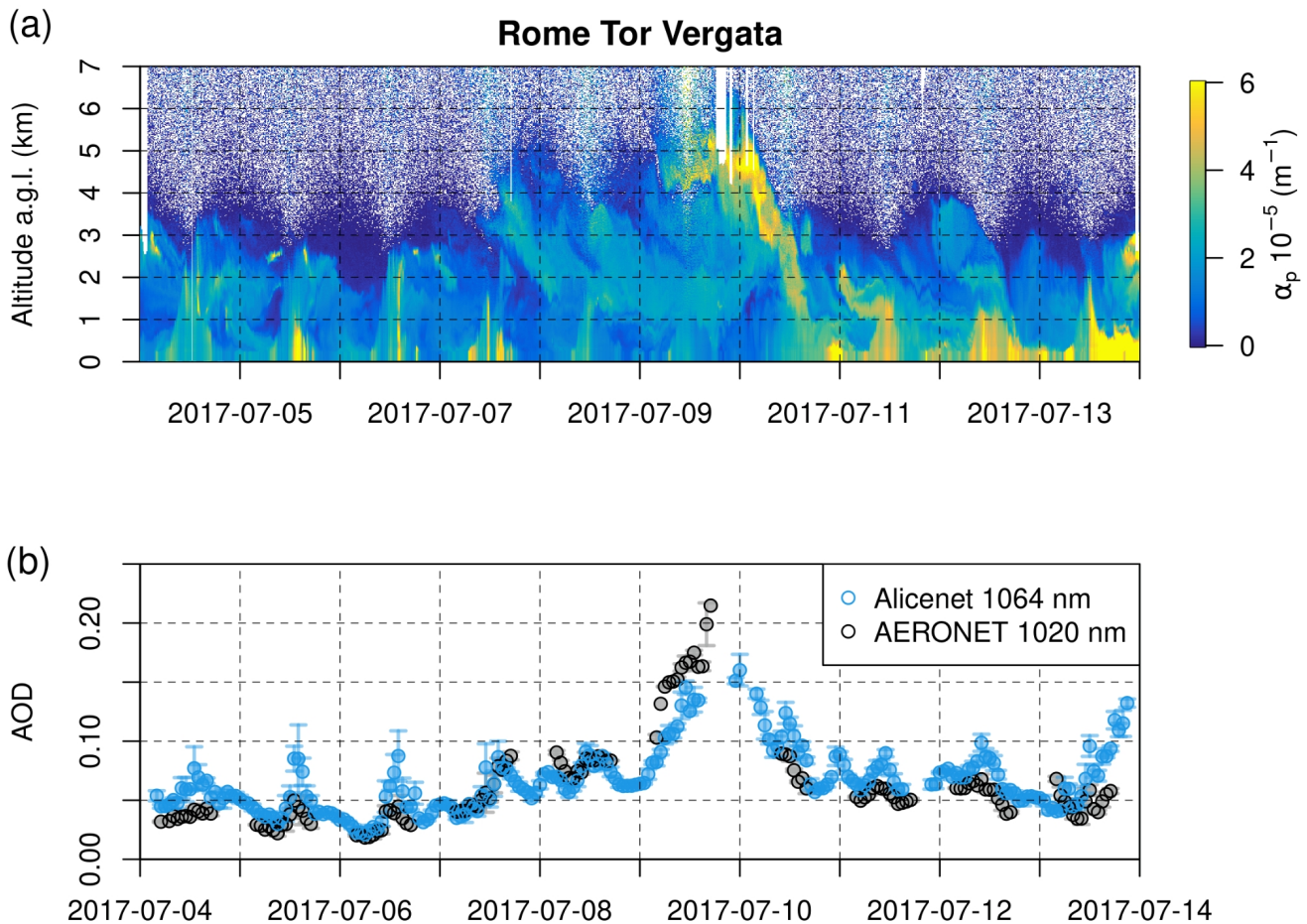
304 The aerosol backscatter and extinction profiles are calculated from the total attenuated backscatter (β_{att}) profile based on the
305 forward Klett inversion (Wiegner and Geiß, 2012; 2014) of Eq. 1. Since both β_p and α_p are unknown in Eq. 1, an assumption
306 on the relationship linking the two variables is necessary to solve the Klett inversion. Within ALICENET, we do not fix an
307 a-priori, vertically-constant extinction-to-backscatter ratio (also referred to as Lidar Ratio, LR), as often done in elastic lidar
308 retrievals. Instead, the aerosol extinction is linked to backscatter through a specific functional relationship ($\alpha_p = \alpha_p(\beta_p)$) already
309 presented and discussed in Dionisi et al. (2018). This was obtained at the CHM15k operating wavelength (1064 nm) based
310 on a large set of simulated optical properties from a continental-type aerosol model. Details on the implementation of the
311 functional relationship within the forward Klett inversion are given in supplement S4.1.

312 It is important to note that, with this procedure, no ancillary data (e.g. co-located sunphotometer-AOD) and no a-priori
313 assumption (e.g. selection of the LR constant value to be used) is needed in the retrieval. Therefore, a-posteriori comparison
314 to co-located sunphotometer-AOD provides a way to check the performance of the ALICENET optical properties retrievals.

315 These comparisons were performed using both short- and long-term datasets thanks to some co-located or closeby
316 AERONET (<https://aeronet.gsfc.nasa.gov/>, last access: 25-07-2024) or SKYNET (<https://www.skynet-isdc.org/>, last access:
317 25-07-2024) sun-photometers. Specific examples are shown in Figs. 6 and 7, respectively.

318 Figure 6a shows the aerosol extinction profiles derived from the Rome-Tor Vergata ALC during the EMERGE-EU field
319 campaign in July 2017 (Andrés Hernandez et al., 2022), while in Fig. 6b the corresponding ALC-derived AOD (blue) is
320 compared with the one measured by the co-located AERONET sun photometer (grey).

321



323

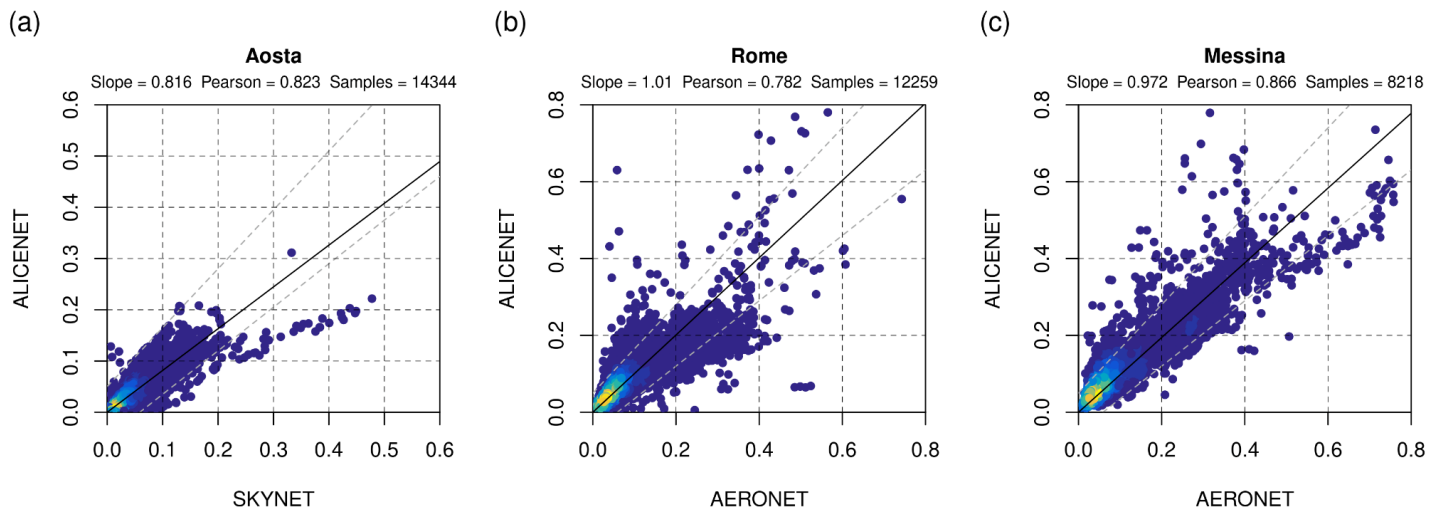
324 **Figure 6:** (a) Aerosol extinction profiles in Rome-Tor Vergata retrieved by the ALICENET inversion during the EMERGE campaign in
 325 July 2017, and (b) comparison between the ALICENET-derived AOD and the co-located AERONET L2 data. Both ALICENET and
 326 AERONET AODs are hourly averaged (error bars are the AOD standard deviations within the averaging interval).

327

328 Figure 6 shows that the time series of the two independent datasets, both averaged at an hourly resolution, agree within the
 329 expected AERONET (Giles et al., 2019) and ALICENET (Sect. 3.3.3) uncertainties. Exceptions are found during days
 330 strongly impacted by transport of Saharan dust (e.g., 9 July 2017). This is expected because, as mentioned, the functional
 331 relationship employed in the inversion was optimised for a continental-type aerosol and does not properly describe the
 332 different backscatter-to-extinction relation in presence of non-spherical particles (e.g., Barnaba and Gobbi, 2001). Also note
 333 that, despite using L2 AERONET data, the maximum sunphotometer AOD value on July 9 corresponds to a cloud-screened

334 time window in the ALC record. The extension of the ALICENET retrieval approach to other aerosol types and relevant
 335 testing is however planned for the future, also taking advantage of the depolarisation measurements capabilities of PLCs
 336 operating within the network.

337 Figure 7 shows a multi-annual (2016-2022), multi-site (Aosta, Roma, Messina) comparison between ALC and
 338 sunphotometer AOD. AERONET L2 data were used in Rome-Tor Vergata and Messina, while SKYNET AOD data in Aosta
 339 were derived taking into account the temperature correction of the POM-02 photometer as described in Uchiyama et al.
 340 (2018). The AOD data were matched in time (measurements within 5 min one from the other) and averaged in time (15 min
 341 average). The overall number of pairs considered in each site is reported in Fig. 7. This comparison shows that the
 342 ALICENET retrieval is able to quantify the actual aerosol load in a variety of conditions. Infact, the number of data pairs
 343 lying within $\pm 0.01 \pm 0.15 \cdot \text{AOD}_{\text{sunphotometer}}$ from the 1:1 line is 84% in Aosta, 73% in Rome, and 70% in Messina. Some
 344 ALC overestimations are mainly due to instrumental noise at higher altitudes, while underestimations are mainly related to
 345 the presence of non continental aerosol types, such as dust and marine particles in Messina, or shallow aerosol layers in the
 346 blind overlap region (i.e., below 225 m a.g.l.), as is the case of Aosta during winter (see Fig. 9). The effects of non
 347 continental aerosol types is better illustrated in the supplement S4.1 (Fig. S4.1.2), where the same data are shown together
 348 with their associated Ångström Exponents.



350 **Figure 7:** Long-term (2016-2022) comparison between the AOD derived by ALICENET (at 1064 nm) and AERONET/SKYNET sun
 351 photometers (at 1020 nm) in (a) Aosta, (b) Rome Tor Vergata, and (c) Messina. Colours refer to the data density. The black line is the
 352 linear fit. Fit slope and Pearson's correlation coefficients are reported in each panel together with the total number of data pairs (samples).
 353 Gray dashed lines delimit deviations of $\pm 0.01 \pm 0.15 \cdot \text{AOD}_{\text{sunphotometer}}$ from the 1:1 line.

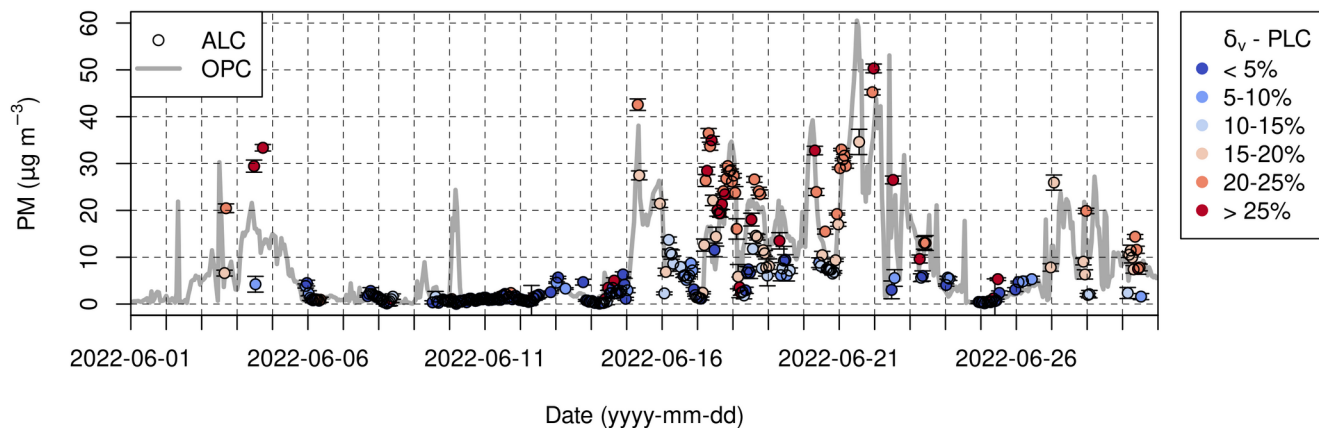
354 3.3.2 Aerosol physical properties

355 Aerosol physical properties such as particle surface area and volume (S_p and V_p) are also derived based on functional
356 relationships linking these to aerosol backscatter and provided in Dionisi et al. (2018). Being of particular interest for AQ
357 applications, aerosol mass concentrations (M_p) can then be derived from the estimated aerosol volume as $M_p = \rho_p V_p$, using
358 an a-priori aerosol density ρ_p . It is worth highlighting that remote sensing aerosol retrievals provide aerosol properties in
359 ‘unperturbed’ atmospheric conditions, i.e., including hygroscopic effects. Conversely, most in-situ instrumentation (as those
360 operating in AQMN in compliance to the EU AQ Directive) generally provide dry particulate matter mass values. Therefore,
361 a RH ‘adjustment’ is necessary when comparing the ALC-based aerosol properties (including mass) to dry in-situ data (e.g.
362 Barnaba et al., 2010). Details on the hygroscopic correction used within ALICENET are reported in the supplement S4.2. In
363 the following, we show both a short- (Fig. 8) and long- (Fig. 9) term comparison between the M_p retrieved by ALICENET
364 using ALC data collected in Aosta and in-situ reference measurements.

365 In Fig. 8, the M_p values at 3500 m a.s.l. extracted from ALC aerosol profiles are compared with the aerosol mass
366 concentrations measured by an OPC at the Testa Grigia - Plateau Rosa observatory (western Alps, 35 km-East of Aosta, see
367 Fig. S4.2.1 in supplement S4 for details on site relative locations) in June 2022. This period was selected because in summer
368 secondary hygroscopic particles from the Po Basin are regularly transported to the western Alps, reaching altitudes > 4 km
369 a.g.l. (Diémoz et al., 2019 a,b). In fact, June 2022 registered both medium-range transport of Po Valley pollution and long-
370 range transport of desert dust to Plateau Rosa. Figure 8 shows the 30-days temporal evolution of the ALC-based M_p (bullets)
371 in the ALC vertical bin 3500 ± 200 m a.s.l. over Aosta and the corresponding values from OPC (grey line). The aerosol
372 density used to derive both ALC and OPC aerosol mass concentrations was 1.2 (1.6) g cm^{-3} in the presence of non-dust
373 (dust-dominated) aerosol mixtures (Diémoz et al., 2019b). Moreover, assuming desert dust as mainly hydrophobic, the
374 hygroscopic correction as described in supplement S4.2 was only applied to ALC data in non-dust conditions. This
375 discrimination was done using the linear volume depolarisation ratio (δ_v) profiles of a co-located PLC and assuming that
376 aerosol mixtures associated with $\delta_v < (>) 15\%$ are dominated by secondary (dust) particles. Overall, Fig. 8 shows that the
377 two mass concentration series exhibit similar time evolution, with good agreement both in low aerosol conditions (e.g. 6-15
378 June 2022), and during transport events increasing the local aerosol load. In the considered period, main transport events
379 were associated with desert-dust intrusions (e.g., 3-5, 18-22, and 27-28 June 2022) and Po Valley pollution advections (e.g.,
380 13-14, and 25-26 June 2022). This result is very promising considering that the horizontal distance between the ALC/PLC-
381 probed column and the Plateau Rosa station is > 30 km and that the in-situ OPC measurements may also be influenced by
382 local dynamics and surface emissions.

383
384
385
386

37
38

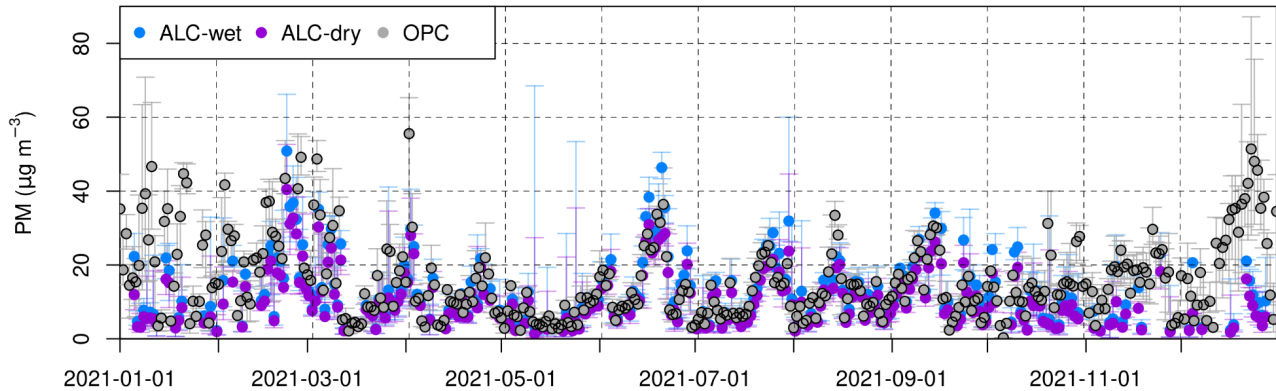


389 **Figure 8:** Aerosol mass concentrations derived in the month of June 2022 from the Aosta ALC (bullets) and from in situ instrumentation
 390 (grey line). In particular, ALC values refer to the vertical layer 3500 ± 200 m a.s.l. and colour code indicates depolarisation values from
 391 the co-located PLC (δ_v). In-situ PM_{10} concentrations were derived from an OPC at the mountain (3500 m a.s.l.) observatory ‘Testa Grigia’
 392 (Plateau Rosa, 35-km from Aosta, data courtesy of Stefania Gilardoni, CNR-ISP).

393

394 A longer comparison for the ALICENET aerosol mass product is reported in Fig. 9. It shows the 1-year (2021) record of
 395 ALC-derived M_p at ground level and the corresponding in situ, surface PM_{10} concentrations derived by OPC measurements
 396 in Aosta downtown, 4 km away from the Aosta ALC (Diémoz et al., 2021). Data are shown in terms of daily median values
 397 and corresponding 25-75 percentiles. To convert volume into mass, the aerosol density was set to 1.5 g cm^{-3} , while to convert
 398 the ALC-derived wet aerosol mass (blue) into dry aerosol mass (purple), the hygroscopic correction (see Eqs. S4.1, S4.2)
 399 was applied using surface-level RH measurements and a constant γ exponent of 0.2. Both ρ_p and γ values are representative
 400 for a mean continental aerosol type, i.e., the one expected to dominate in Aosta. As can be observed, the ALICENET
 401 retrieved M_p is able to reproduce the variability of the in-situ measured PM_{10} , with some underestimations in the winter
 402 months. We investigated these underestimations further and found these are mainly attributable to: a) the shallow (i.e., few
 403 tens of metres), frequent temperature inversions occurring during winter in the Alpine valleys and capping aerosols in the
 404 lowermost levels (e.g., Giovannini et al., 2020), and b) the higher wintertime local emissions in the urban site of Aosta
 405 downtown with respect to the semi-rural site where the ALC is operating (Diémoz et al., 2019b).

406



408 **Figure 9:** One-year (2021) dataset of surface aerosol mass concentrations as derived by the ALICENET ALC inversion and by OPC
 409 measurements in Aosta. Data refer to daily median values (points) and relevant 25-75 percentiles (vertical bars). ALC-based data are both
 410 those derived from the ALICENET retrieval (wet) and corresponding ones further corrected to dry values (see the supplement S4).
 411

412 3.3.3 Estimated uncertainty of aerosol properties retrievals

413 The previous sections describe the ALICENET efforts to exploit the great potential of ALC in providing quantitative
 414 aerosol-related geophysical parameters, and demonstrate the good performances of the current algorithms. Nonetheless, due
 415 to several factors also discussed above, the expected uncertainties associated with the output products range from 20% for
 416 the attenuated backscatter (product L2 in Fig.1) to 50% for the aerosol mass (L3 in Fig. 1). The main factors are listed
 417 hereafter.

418 1) the instrumental noise of the signal. This factor depends on the instrument status and mainly impacts the retrievals in the
 419 middle-upper troposphere.

420 2) the overlap correction applied to the signal. As discussed, this factor is critical in the lowermost levels and accurate
 421 instrument-specific, overlap-correction models are necessary to derive quantitative information in the first 800 m. Accuracy
 422 of the retrievals in this vertical region depends on the statistical and physical representativeness of the ensemble of overlap
 423 functions from which the overlap model is derived (supplement S2).

424 3) the variability of the instrument calibration coefficient. This third factor (see Sect. 3.2), directly impacts the accuracy
 425 of β_{att} . For example, it is found by error propagation that changes of 30% in the instrument calibration coefficient (which are
 426 quite usual in some ALICENET and E-PROFILE stations) translates into a variability in β_{att} up to 20%.

427 4) the accuracy of the functional relationships used in ALICENET to link the aerosol backscatter to the other aerosol
428 properties, impacting the estimation of α_p , S_p , V_p , M_p and, to a lesser extent, β_p . This factor strongly depends on the actual
429 aerosol conditions: the functional relationships can give a good estimate of the aerosol properties in presence of continental
430 aerosols, while in presence of non-continental particles they are less accurate (a relative error of 30-40% was derived by
431 Dionisi et al., 2018). As mentioned, extension of the ALICENET approach to include other aerosol types is foreseen for the
432 next future. In particular, exploitation of the PLC depolarisation profiles for aerosol-typing will drive the selection of
433 aerosol-type specific functional relationships (e.g. Gobbi et al., 2002).

434 Concerning the retrieval of aerosol mass concentrations, the assumed particle densities are a major source of uncertainty, and
435 the accuracy of the retrieval depends on the possibility to better constrain the aerosol density profiles, e.g., through ancillary
436 data, including depolarisation information.

437 Overall, the above factors result in instrument-, time- and range-dependent uncertainties of the ALC-based aerosol optical
438 and physical properties. The expected uncertainty with an optimal SNR up to at least 7 km a.g.l., an overlap error < 10% in
439 the lowermost levels, and in presence of continental aerosol types is of 20% for β_{att} , 30-40% for AOD, reaching 50% for
440 aerosol mass.

441

442 **3.4 The ALICENET automatic Aerosol Layer DetectIoN algorithm (ALADIN)**

443 As already mentioned, a main advantage of ALCs is their ability to operate continuously, which allows detecting and
444 tracking the variability of the aerosol vertical stratifications at multiple timescales using aerosol as passive tracers. This
445 information can be beneficial for several sectors, among which AQ and meteorology (e.g., Moreira et al., 2019; Ravnik et
446 al., 2024; Körmöndi et al., 2024), aviation (e.g., Osborne et al., 2019; Salgueiro et al., 2023), atmospheric research (e.g.,
447 Jozef et al., 2024).

448 Commonly identified atmospheric stratifications based on ALC data analysis include the Atmospheric Boundary Layer and
449 the Mixed Layer (ABL and ML, respectively, e.g., Poltera et al., 2017; Kotthaus et al., 2020; Caicedo et al., 2020), and
450 lofted aerosol layers in the free troposphere (e.g., Adam et al., 2020). The ABL is a thermodynamic layer connected to the
451 Earth's surface and capped by a temperature inversion, while the ML is an ABL sublayer mixed by turbulent fluxes (Stull,
452 1988; Kotthaus et al., 2023).

453 However, it should be noticed that aerosols are 'delayed' tracers of atmospheric dispersion processes and may not always
454 consistently represent the thermodynamic state of the atmosphere (Haeffelin et al., 2012). The tracking of thermodynamic
455 layers through aerosol lidars can be complicated by superimposing phenomena such as large-to-medium scale advections,
456 natural and anthropogenic emissions, particle physico-chemical transformations. These processes may remove or transport
457 particles in specific atmospheric ranges (e.g., Collaud Coen et al., 2018; Diémoz et al., 2019a), modulate the daily cycle of
458 aerosol profiles (e.g., Diémoz et al., 2021), form aerosol layers within and above the ABL (e.g., Curci et al., 2015; Sandrini
459 et al., 2015), thus decoupling the aerosol-related and thermodynamic stratifications. This decoupling is expected to be further

460 enhanced over complex terrain (e.g., Serafin et al., 2018) and/or over regions affected by multiple natural and anthropogenic
461 sources, as is the case of the Italian territory.

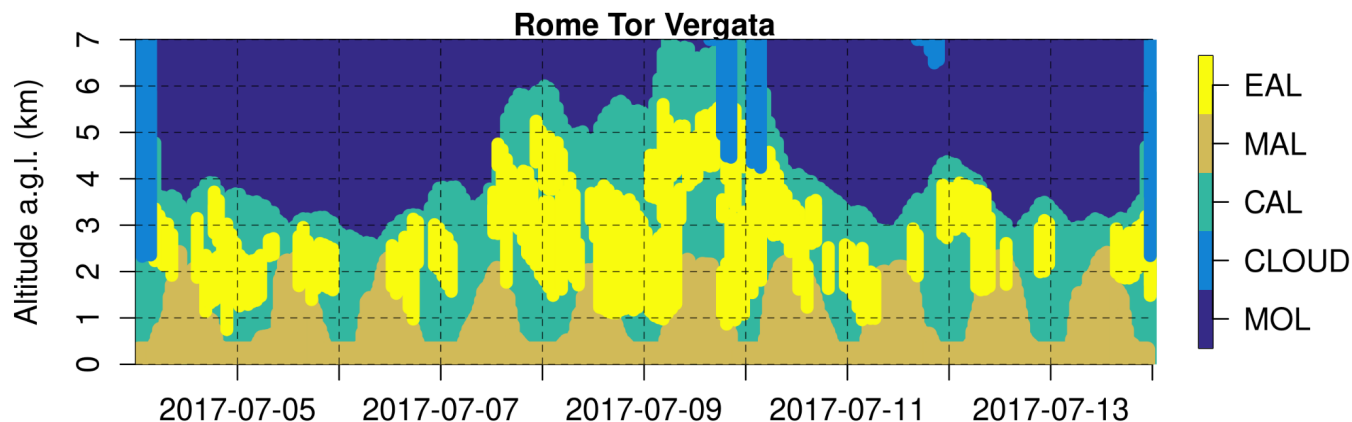
462 For all these reasons, the choice for aerosol layers detection and naming in ALICENET was to keep a clear link to the
463 aerosol field allowing its identification, avoiding a terminology traditionally based on thermodynamics. In particular, we
464 develop a novel Aerosol LAYer DetectIoN (ALADIN) tool to automatically derive aerosol layering information from
465 ALCs/PLCs across the network, this targeting the following aerosol layers:

- 466 1. the Continuous Aerosol Layer (CAL): it is the layer extending from the ground level and characterised by the
467 continuous presence of aerosols;
- 468 2. the Mixed Aerosol Layer (MAL): it is a CAL sublayer within which aerosols are mixed by surface-driven turbulent
469 fluxes;
- 470 3. Elevated Aerosol Layers (EALs): they are lofted aerosol layers which lie above the MAL, and either within or
471 above the CAL.

472 Within ALADIN, each layer type (CAL, MAL, and EALs) is detected from ALC/PLC L2 data using a specific methodology.
473 The CAL is determined by comparing the aerosol and the molecular β_{att} profiles. The identification of the MAL is based on
474 Dynamic Time Warping (DTW, Giorgino et al., 2009) and variance analyses of the ALC profiles. The detection of EALs is
475 performed with Continuous Wavelet Transform (CWT, Du et al., 2006) and iterative techniques. Full details on the
476 ALADIN procedures, as well as a schematic description of the ALADIN processing flow are reported in supplement S5.

477 Figure 10 shows the ‘layering mask’ corresponding to the same ALC data shown in Fig. 6. It includes the ALADIN output
478 discriminating the CAL, MAL, and EALs, plus the aerosol-free (i.e., molecular, MOL), and cloud-screened (CLOUD)
479 regions as inferred from the overall ALICENET processing. In this episode, the EALs above 3 km a.g.l. are mostly due to
480 minor (July 7-8 and 10-11) and major (July 9) Saharan dust intrusions, while the ones between 1-3 km a.g.l. to fire plumes
481 (e.g., July 11; Andrés Hernandez et al., 2022) and/or to aerosol formation and growth within the residual layer during
482 nighttime (e.g., July 5-6).

483
484
485
486
487
488
489
490
491
492



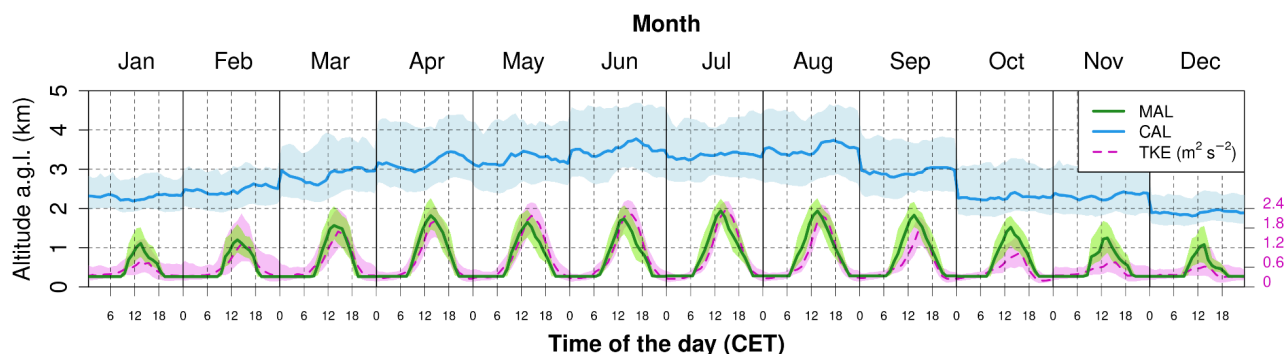
495 **Figure 10:** Aerosol layering mask derived from the ALADIN processing on the CHM15k operating in Rome - Tor Vergata in the same
 496 period presented in Fig. 6. The mask discriminates the following layers: the continuous aerosol layer (CAL), the mixed aerosol layer
 497 (MAL) and elevated aerosol layers (EALs). Aerosol-free (i.e., molecular, MOL) and cloud-screened (CLOUD) regions as identified in the
 498 overall ALICENET processing are also shown.

499

500 Further discrimination of aerosol layers in terms of aerosol type could be derived exploiting PLC δ_v profiles. In fact, the
 501 inclusion of the PLC depolarisation information within the ALICENET processing is in progress, this representing a first
 502 step to automate the aerosol typing capacity within the network (thus complementing the aerosol layer typing capacity from
 503 more complex lidar systems, e.g., Nicolae et al., 2018; Córdoba-Jabonero et al., 2018).

504 Routine application of the automated ALADIN tool on a daily basis also allows to get statistics of vertical aerosol
 505 stratifications in the atmosphere. An example of this long-term application is presented in Figure 11, which shows the
 506 monthly- and daily-resolved cycle of MAL and CAL heights over Rome-Tor Vergata derived from the 2016-2022 ALC
 507 dataset (continuous lines are median values while shaded areas represent 25th-75th percentiles). Figure 11 clearly shows the
 508 marked yearly cycle of the CAL height (minimum in winter and maximum in summer), due to the increased convection and
 509 photochemistry in the warmest months (e.g. Barnaba et al., 2010). As expected, all over the year the MAL shows a marked
 510 daily cycle, with maximum heights in summer (about 2 km thick in July-August) doubling those in winter (about 1 km in
 511 December-January). A similar statistics of turbulent kinetic energy (TKE) from a co-located ultrasonic anemometer
 512 (magenta lines) is also reported as a proxy for convection, which is the main driving factor of the MAL temporal evolution.
 513 Note that in this Figure the time axis is reported as Central European Time (CET) to better highlight the diurnal variability of
 514 the addressed quantities.

515



517

518 **Figure 11:** Monthly and daily resolved statistics (median, and 25-75 percentiles as shaded dashed areas) of the MAL and CAL heights
 519 (left y-axis) derived from the ALADIN tool application over the multi-annual (2016-2022) dataset of the CHM15k in Rome Tor Vergata.
 520 Similar statistics of the turbulent kinetic energy (TKE) derived from a co-located ultrasonic anemometer (violet) are also plotted (right y-
 521 axis) as a proxy of convection intensity and timing.

522

523 A follow up work presenting a more detailed multi-annual analysis of the ALC-based aerosol properties and layering in
 524 selected ALICENET sites from North to South Italy, in synergy with in-situ aerosol measurements and model (ERA5,
 525 CAMS) products, is currently in progress (Bellini et al., 2024, in preparation).

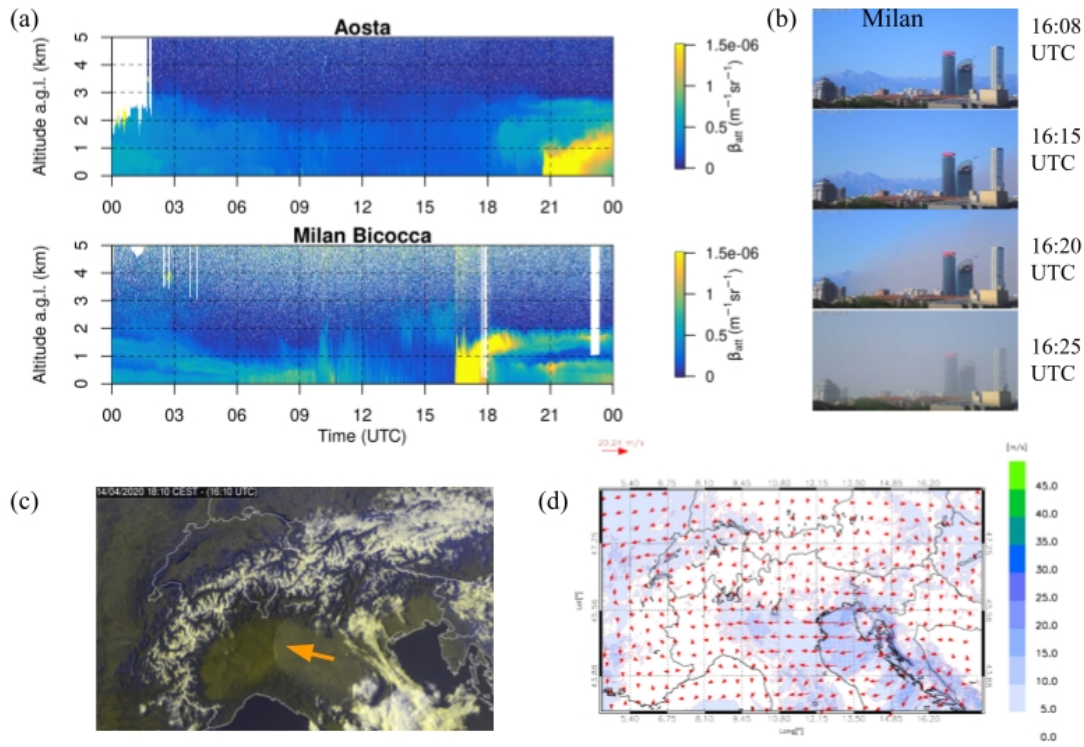
526 4. Potential of 4D near-real time aerosol monitoring

527 A main advantage of lidar-ceilometers networks is their continuous, near real-time monitoring capability. In fact,
 528 ALICENET has been already exploited in past events to follow the evolution and characterise specific aerosol transport
 529 features and/or to quantify the impact of aerosol dynamics on local aerosol concentrations, mostly in synergy with other
 530 tools and measuring techniques as in-situ aerosol observations, ground-based passive remote sensors, satellites or models
 531 (Gobbi et al., 2019; Diémoz et al., 2019a,b; Di Bernardino et al., 2021; Rizza et al., 2017, 2022; Tositti et al., 2022; Andres
 532 Hernandez et al., 2022). This section describes, through some recently recorded showcases, the potential of this near real
 533 time 4-dimensional ALICENET monitoring at the national scale, particularly useful for nowcasting, warnings and alerts in
 534 case of noteworthy events.

535 4.1 Po Valley local dust front (14 April 2020)

536 In a previous study (Diémoz et al., 2019a,b), the operational use of ALICENET provided observation-based evidence of the
 537 export of pollutants from the Northern Italy Po Valley to surrounding areas. The phenomenon, previously observed by lidar
 538 profiling performed at the EC-JRC in Ispra (about 60 km northwest of Milan, Barnaba et al., 2010), was further analysed

539 and quantified thanks to the ALICENET combination of sites (Milan and Aosta, i.e., within and at the border of the Po
 540 Valley). That study demonstrated that such pollution-rich advections markedly affect PM-related AQ even in the ‘pristine’
 541 mountain environments mainly transporting hygroscopic particles of secondary origin. However, transport of particles of
 542 primary origin (particularly from soil-related sources) across the Po Valley has been also observed, particularly during dry
 543 periods. Figure 12 shows an example of such events (14 April 2020), largely impacting regional AQ and visibility.
 544



546
 547 **Figure 12:** (a) Total attenuated backscatter profiles at Aosta and Milan-Bicocca sites on 14/04/2020; (b) central Milan webcam (Source:
 548 Arzaga meteorological observatory, <https://www.osservatorioarzaga.it/>) showing the rapid decrease of visibility on 14/04/2020 (from top
 549 to bottom: 16:08, 16:15, 16:20, 16:25 UTC), (c) Po Valley satellite true colour image (14/04/2020 18:10 UTC; Credits: EUMETSAT) with
 550 indication of the regional dust front (orange arrow), and (d) 10 m wind speed and direction simulated by WRF over North Italy
 551 (14/04/2020 17:00 UTC, data courtesy of Stefano Federico CNR-ISAC) illustrating the extension of the gust and wind fronts. The arrival
 552 of the dust front in Milan at 16:20 UTC and in Aosta at 20:40 UTC is clearly visible from ALC profiles in panel a.
 553

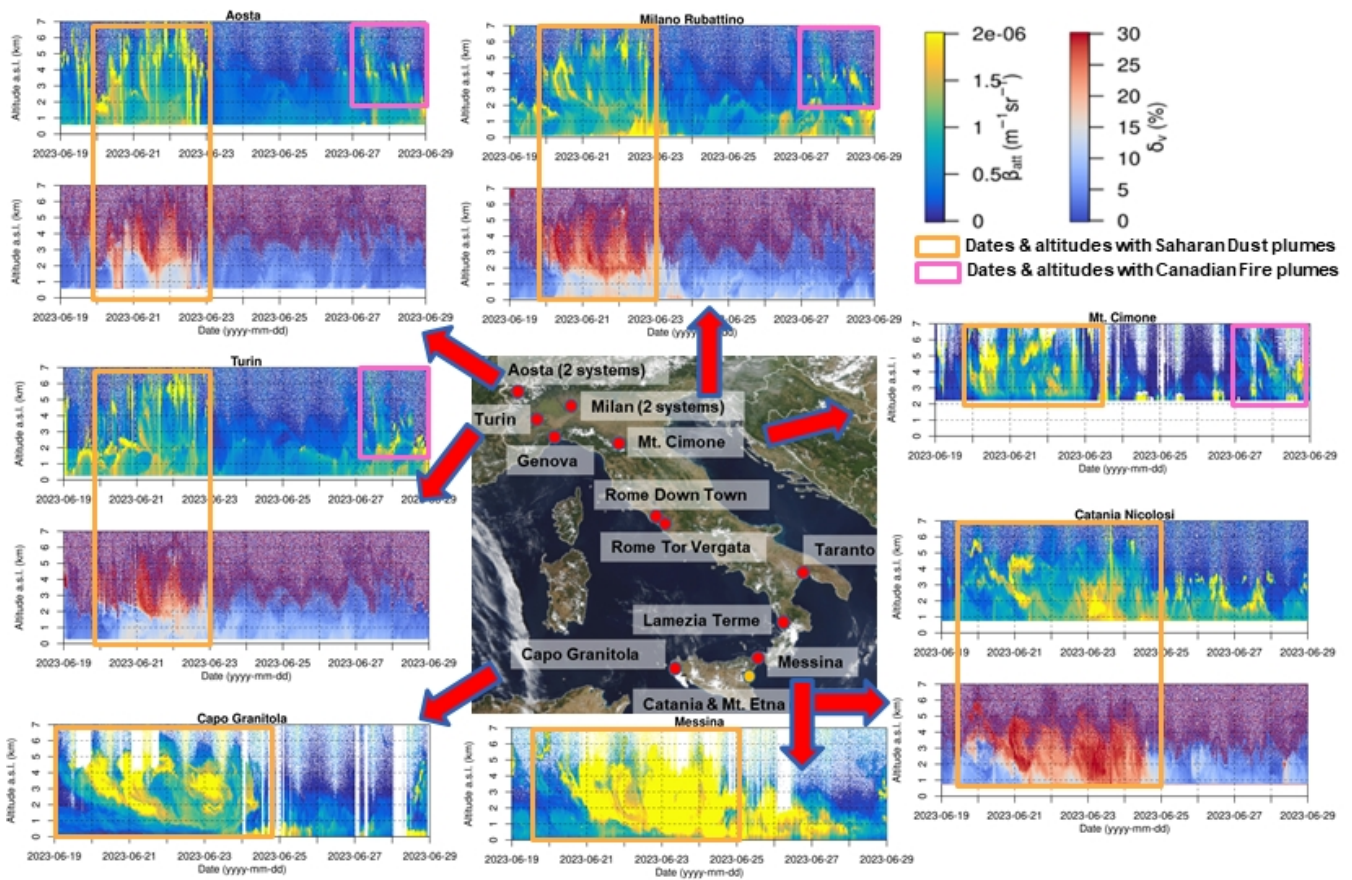
554 This episode was due to an extended (about 100 km) gust front originating from the cold and intense Bora winds from East,
 555 as well as to anomalous dry conditions affecting Europe in April 2020. Resuspended, soil-originated particles from the

556 cultivated fields were transported across the whole Po Valley as also visible from space (Fig. 12c). ALC profiles (Fig. 12a)
557 well captures the timing of the plume's arrival in Milan (as also seen from central Milan webcams, Fig. 12b) and show the
558 vertical extent of the particle-rich layer associated with the episode. As also revealed by satellite measurements (Fig. 12c)
559 and model simulations (Fig. 12d), after impacting the Milan area, the plume continued to travel westward and was detected
560 by the ALC in Aosta 4 hours later, indicating a wind speed > 12 m/s.

561 **4.2 Advection of Saharan dust and Canadian fire plumes over Italy (19-28 June 2023)**

562 The Mediterranean area is frequently affected by the transport of desert dust from North Africa and the Middle East (e.g.,
563 Barnaba and Gobbi, 2004; Querol et al., 2009; Basart et al., 2012a; Greilinger et al., 2019; Gama et al., 2020). In Italy, these
564 events are estimated to reach the ground on 10% (Northern regions) to over 30% (Southern regions) of the days in a year,
565 and to impact on surface daily-mean PM₁₀ concentrations with 10-15 µg/m³ (Barnaba et al., 2022). Transport of fire plumes
566 from global-to-medium distances is also an important contributor to aerosol loads in Europe. A significant contribution is
567 given by forest fires regularly developing during boreal summers in Canada (e.g., Ceamanos et al., 2023; Shang et al., 2024),
568 and a major contribution from agricultural fires in Eastern Europe and Russia has also been detected over the continent,
569 particularly in spring and summer (Barnaba et al., 2011). Summer 2023 was particularly impacted by multiple episodes of
570 severe wildfires in central Canada. Almost 480 megatonnes of carbon were emitted, resulting in a major impact on AQ
571 across Canada and the Northern US. The plumes have also been observed to be regularly transported towards Europe
572 (<https://atmosphere.copernicus.eu/copernicus-canada-produced-23-global-wildfire-carbon-emissions-2023>, last access: 6-3-
573 2024). Figure 13 shows a composite of measurements collected at multiple ALICENET sites across the country during a 10-
574 days period (19-28 June 2023) affected by both desert-dust (time-altitude windows identified by orange boxes) and forest-
575 fire plumes (time-altitude windows identified by magenta boxes). More specifically, this period was characterised by the
576 intrusion of Saharan dust to Southern to Northern Italy (19-24 June 2023), followed by the transport of Canadian fire plumes
577 over Central and Northern Italy (27-28 June 2023). The ALC profiles (β_{att} and δ_v) at the 7 selected ALICENET sites (central
578 panel in Fig. 13) allow to follow the spatio-temporal evolution of the different aerosol layers and identify the relevant aerosol
579 type. The Saharan dust layers were firstly observed over South-West Italy (Capo Granitola, June 19 in the morning), then
580 moving westward to Messina and Catania (June 19, afternoon), and northward to Turin, Aosta, Milano, Mt. Cimone, where
581 the dust plume is detected in the evening. All over Italy, the dust plume affects atmospheric layers up to 7 km altitude,
582 reaching down to the surface on June 20. In fact, the PLC systems clearly indicate the presence of irregularly-shaped mineral
583 particles aloft (depolarisation values $\delta_v > 30\%$) and mixing with local (mainly spherical) particles, with $\delta_v \sim 10-20\%$ when
584 reaching the lowermost levels.

585
586



587

588

589 **Figure 13:** Vertical profiles of total attenuated backscatter β_{att} (for both ALCs & PLCs) and volume depolarisation δ_v (for PLCs) as
 590 recorded at selected, North-to-South ALICENET sites in the period 19-28 June 2023, affected by Saharan dust and Canadian fire plumes
 591 (orange and magenta boxes, respectively).

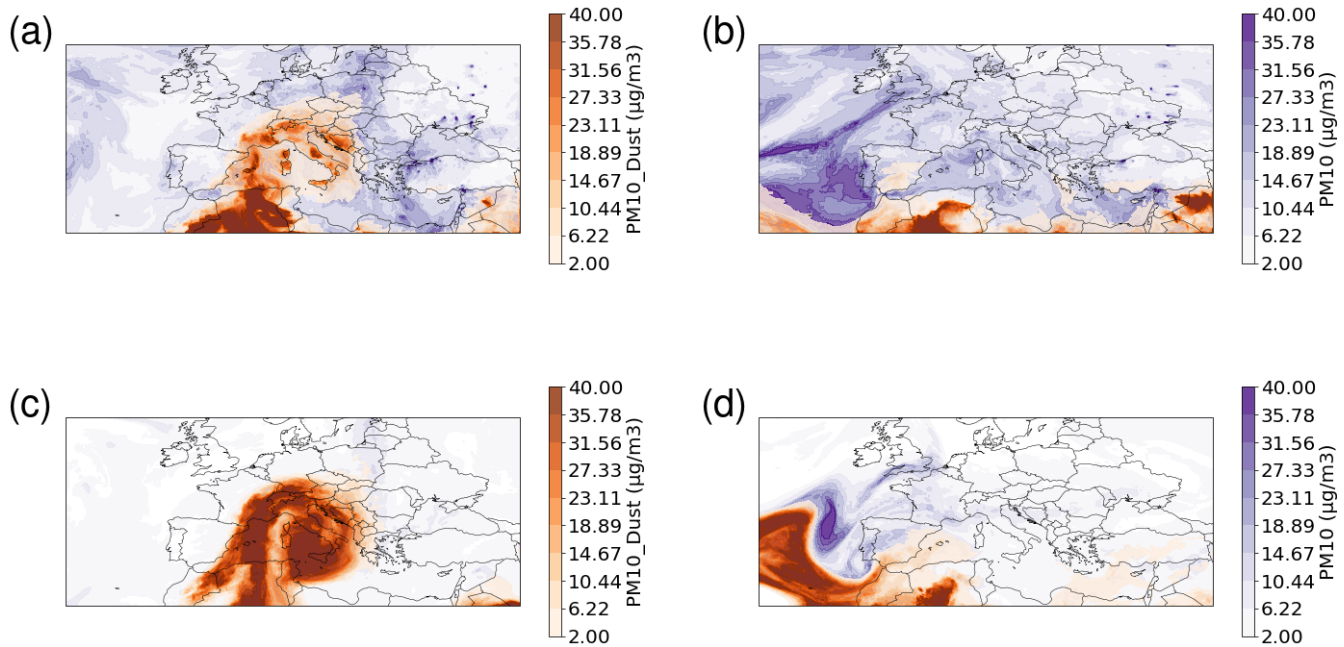
592

593 The Canadian fire plumes were firstly observed by ALICENET systems operating in North-Western Italy (Aosta, Turin) on
 594 27 June 2023 in the range 2-7 km a.s.l. Then travelled through the whole Po Valley, being clearly observed in Milan and Mt.
 595 Cimone. Being mainly composed of processed particles, these long-range transported fire plumes do not show increased
 596 depolarisation, and appear as thinner aerosol layers with respect to the ones typically associated with dust layers. These
 597 vertically resolved measurements well complement the information that can be gathered from satellites. For instance, a
 598 comparison between ALICENET data and MSG and Metop retrievals was conducted with respect to the dust event (e.g.,
 599 <https://vuser.eumetsat.int/resources/case-studies/dust-transport-from-the-sahara-to-the-mediterranean>, last access: 6-3-2024).
 600 At the same time, vertical aerosol profiling also provides an observational verification of the picture that can be obtained by
 601 modelling tools. In this respect, Fig. 14 shows the CAMS EU forecast maps (Ensemble model) for two dates within the
 602 temporal window addressed, i.e.: 22/06/2023 (dust intrusion, left panels) and 27/06/2023 (Canadian fires, bottom panels), at

55

56

603 two altitude levels (100 and 3000 m a.g.l., top and bottom panels respectively). The horizontal evolution of the aerosol
 604 advections qualitatively agrees with the ALICENET observations. It is more difficult to correctly model the aerosol vertical
 605 distribution, due to both their coarse vertical resolution and simplified parameterizations of the aerosol-related atmospheric
 606 processes (e.g., Koffi et al., 2016). Indeed, remote sensing observations by ALC/PLC represent an added value for both AQ
 607 monitoring and modelling. In fact, specific efforts are currently ongoing in the assimilation of ceilometer information into
 608 the IFS (Integrated Forecasting System)/CAMS (e.g., the H2020 CAMs AERosol Advancement (CAMAERA) Project,
 609 <https://camaera-project.eu/>, last access: 25-07-2024).

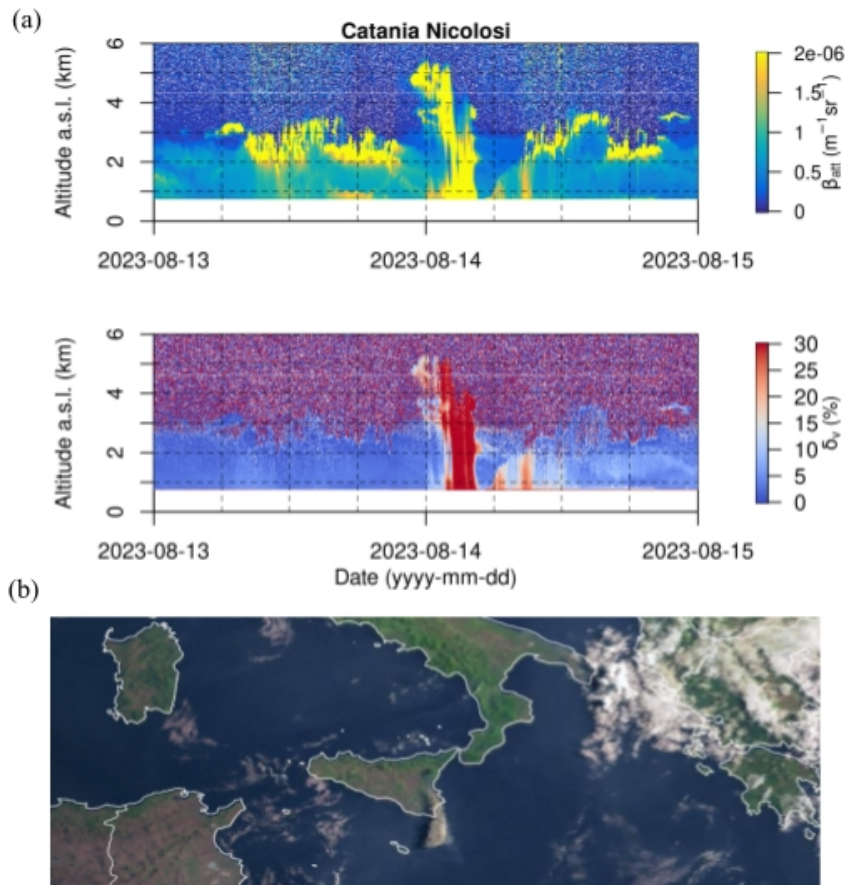


611 **Figure 14:** CAMS EU forecast of the total PM10 and PM10-dust component concentrations during the desert dust (22/06/2023 00:00 UTC
 612 - left panels) and the Canadian fires (27/06/2023 21:00 UTC - right panels) events of Figure 13, top (bottom) panels referring to 100 m
 613 (3000 m) altitude.

614
 615 **4.3 Aerosol particles from the Mt. Etna eruption (13-14 August 2023)**

616 A recent showcase from the Etna volcano eruption is reported in Figure 15 to highlight the important information that
 617 ALC/PLC observations can provide in volcanic areas to complement in situ, satellite-based and modelling data (e.g.,

618 Corradini et al., 2018, Scollo et al., 2019, Bedoya-Velásquez et al., 2022) . During the night between 13 and 14 August 2023,
619 this Europe's most active volcano erupted, its Southeast Crater emitting a volcanic cloud that the PLC in Nicolosi detected to
620 reach up to 5 km at 21 UTC (Fig 15a). On August 13, at 20:41 UTC, a Volcano Observatory Notice for Aviation (VONA)
621 was issued by INGV (https://www.ct.ingv.it/Dati/informative/vona/VONA_Etna_202308132041Z_2023005708E01.pdf, last
622 access: 06-03-2024) with a 'red alert' for aviation. VONA are short, plain-English messages aimed at dispatchers, pilots, and
623 air-traffic controllers to inform them of volcanic unrest and eruptive activity that could produce ash-cloud hazards. In fact,
624 flights serving Catania were halted. The most intense phase of the eruption occurred between 01:40-02:30 UTC, when PLC
625 depolarisation reached values > 40% indicating a predominance of irregular ash particles. The ash plume was then observed
626 to rapidly reach the ground, while moving southward in the Mediterranean Sea (Fig 15b). In fact, less than 5 hours after the
627 beginning of the eruption the plume was detectable east of Malta. In agreement with the ALC record, the VONA issued by
628 INGV at 05:54 UTC indicates that no ash plumes were produced and that the volcanic ash was confined in the summit areas
629 of the volcano, this corresponding to an orange Aviation colour code
630 (https://www.ct.ingv.it/Dati/informative/vona/VONA_Etna_202308140554Z_2023005808F01.pdf, last access: 06-03-2024).
631



633 **Figure 15:** (a) Total attenuated backscatter, β_{att} , plus volume depolarisation, δ_v , profiles observed at the ALICENET Etna Nicolosi site on
 634 13-14/08/2023; (b) METEOSAT Natural Colour Enhanced RGB (SEVIRI) image referring to 14/08/2023, 05:15 UTC (Credits:
 635 EUMETSAT).

636

637 5 Conclusions and and future perspectives

638 In this work we present ALICENET, the Italian network of automated lidar-ceilometers (ALCs) operating from North to
 639 South across the peninsula. It is a cooperative network set up by CNR-ISAC in 2015, and currently running with active
 640 contributions from several regional EPAs, Universities, Research Centres and private companies. The network contributes to
 641 fill an Italian observational gap at the EU level, where most Member States generally run extended ALC networks managed
 642 by national meteorological agencies (e.g. the German weather service, DWD, running over 100 instruments,
 643 https://www.dwd.de/EN/research/observing_atmosphere/composition_atmosphere/aerosol/cont_nav/aerosolprofiles.html,

61
 62

644 last access 25-07-2024). Since its set up, the ALICENET network kept expanding (Table 1), and currently covers very
645 different environments (urban, coastal, mountainous and volcanic areas), thus providing information in a large spectrum of
646 atmospheric conditions and aerosol regimes. ALICENET promoted a standardisation of instruments and an homogeneous
647 data processing specifically developed within the network. It mainly runs single-channel ALCs (CHM15k systems by Ott
648 Hydromet) but is progressively introducing polarisation-sensitive systems (PLCs) recently commercialised by Vaisala
649 (CL61) to further exploit the ability of these systems to discriminate among aerosol types. Since the beginning of the
650 ALICENET activities, particular care has been devoted to data retrievals and exploitation, this also taking advantage of
651 technical/scientific exchanges within European initiatives, such as the EC Cost Actions TOPROF (2013-2016) and PROBE
652 (2019-2024), the ongoing EUMETNET program E-PROFILE (2020-2028) and the EC H2020 Project RI-URBANS (2021-
653 2025). In this context, ALICENET developed a specific, centralised and automated data processing chain with associated
654 data quality control (QC) procedures, as presented in detail in this work. The data processing steps were either refined from
655 previously published work (e.g. Hervo et al., 2016, Dionisi et al., 2018), or are completely new, as the automatic aerosol
656 layers detection algorithm (ALADIN). Overall, the processing chain includes signal correction and calibration procedures
657 (Sects. 3.1, 3.2), the aerosol properties inversion (Sect. 3.3), and the identification of vertical stratifications (Mixed,
658 Continuous and Elevated Aerosol Layers, MAL, CAL and EALs, respectively, Sect. 3.4). Output products with different
659 levels of complexity and associated uncertainties are thus provided (Fig. 2). These range from more basic L1 quantities (as
660 the Range-Corrected Signal, RCS, and, where applicable, depolarisation, δ_v), through the L2 total attenuated backscatter β_{att}
661 to the L3 aerosol optical (β_p , α_p and thus AOD) and physical (S_p , V_p , and M_p) properties plus vertical layering.
662 Level 1 and Level2 products are provided in near real time on a dedicated website (<https://www.alice-net.eu/>, last access: 25-
663 07-2024), while L3 products are obtained offline and are currently only available upon request. Examples of product types
664 are reported in Sect. 3 and 4. For L3 products, this work also includes direct comparisons with relevant, independent data
665 (in-situ or remote sensing, depending on the variable addressed), showing that the ALICENET data processing is able to
666 provide robust and quantitative aerosol information, within the discussed limits of the data accuracy (Sect. 3.3.3). In fact,
667 long-term comparisons of aerosol mass retrievals with surface PM_{10} data show mean discrepancies of 35%, while AOD
668 comparisons to thousands of relevant data points from co-located sun photometers show correlation coefficients > 0.8 and fit
669 slopes ranging between 0.8-1.0, depending on the site location.

670 Efforts to evaluate the ALICENET retrieval performances are constantly performed as well as comparisons to different
671 inversion approaches and tools. For example, a preliminary algorithm intercomparison exercise was recently performed
672 within PROBE to evaluate differences in the outcomes produced by different national networks in the EU (namely:
673 ALICENET - Italy, MetOffice - UK, V-PROFILE - Norway, DWD - Germany; Osborne et al., 2024). An additional analysis
674 of the ALICENET L3 products is currently in progress based on multi-annual datasets of selected ALICENET systems
675 located across Italy and relevant comparisons to independent data and models (Bellini et al., 2024, in preparation).

676 Next steps foreseen within the network are: a) a better characterisation of the instruments artefacts and calibration, b) the
677 extension of the ALICENET ALC retrieval methodology to different aerosol types, c) the development of a full retrieval for

678 PLCs (CL61), further exploiting the depolarisation information to identify aerosol types. Since the CL61 operates at a
679 different wavelength with respect to CHM15k, the evaluation of water vapour absorption corrections (e.g., Wiegner and
680 Gasteiger, 2015), and the definition of new, wavelength specific functional relationships (e.g. Dionisi et al., 2018) to be used
681 within the data inversion process are also required and will be explored. The feasibility of a regular dissemination of
682 ALICENET L3 products via the network website in addition to the near-real time L1 and L2 ones is also under evaluation.
683 Overall, ALICENET represents a valuable resource to complement the aerosol observational capabilities in Italy with the
684 unique capacity of continuous 4D monitoring. The maturity of both instrumental technologies and data processing tools as
685 the ones described here suggest that ALC/PLCs could fruitfully contribute to aerosol measurements within European
686 Research Infrastructures (e.g. ACTRIS) and/or air quality monitoring networks (AQMNs).

687 At the national level, ALICENET also intends to bridge a gap between the research-oriented and the operational use of
688 active aerosol remote sensing in several sectors, among which: a) air quality (AQ), b) radiative budget/solar energy, c)
689 aviation safety, thus representing a good example of earth observation science applications for society. Its outputs were
690 already proven to be also useful in validation of models and satellite products.

691 Of particular interest for the AQ sector are the abilities of the ALC/PLC-based ALICENET data to: i) automatically identify
692 medium-to-long range aerosol advections and estimate the relevant contribution to surface PM10 concentrations, and ii)
693 provide continuous information on particulate matter layering, including the Mixing Aerosol Layer (MAL), i.e. on the
694 atmospheric volume in which locally emitted particles are diluted (e.g., Kotthaus et al., 2023), and the Elevated Aerosol
695 Layers (EALs) reaching the surface. The effectiveness of using these ALC/PLC abilities in support of standard AQMNs is
696 being currently explored within the ongoing EC H2020 Project RI-URBANS, aimed at developing an air quality monitoring
697 system that complements those currently available. In this framework, tests of upscaling the ALICENET tools to other urban
698 sites in the EU are in progress (e.g., Barnaba et al., 2024). Concerning the other applications mentioned above, the
699 continuous ALC-based information on the aerosol properties vertical distribution and layering is useful to better estimate the
700 relevant radiative effects (beneficial for example within an operational short-term solar forecasting system based on a
701 multisensor approach, e.g. Papachristopoulou et al., 2024), for validation of/assimilation in models (e.g. Chan et al., 2018;
702 Valmassoi et al., 2023), or for the provision of near-real time alerts for aviation safety during specific extreme events such as
703 desert dust storms and volcanic eruptions (e.g., Papagiannopoulos et al., 2020). Continuous aerosol monitoring capabilities
704 of ALC/PLC systems and availability of relevant long-term records is also expected to be particularly important in the
705 verification of satellite aerosol products including vertical layering (e.g., Janicke et al., 2023), considering that aerosol
706 vertical profiles and planetary boundary layer are recognised as priority targeted observable for space-based Earth
707 observation programs (e.g. NASEM, 2018) and that the joint ESA-JAXA mission EarthCare with a lidar instrument onboard
708 was recently successfully launched (e.g., van Zadelhoff et al., 2023).

709
710

- 711 **List of acronyms**
- 712 **ABL: Atmospheric Boundary Layer**
- 713 **ACTRIS: Aerosol, Clouds, and Trace Gases Research Infrastructure**
- 714 **AERONET: Aerosol Robotic Network**
- 715 **ALADIN: Aerosol LAYer DetectIoN algorithm**
- 716 **ALC: Automated Lidar-Ceilometer**
- 717 **ALICENET: Automated Lidar-CEilometer NETwork**
- 718 **AQ: Air Quality**
- 719 **AQMN: Air Quality Monitoring Network**
- 720 **AOD: Aerosol Optical Depth**
- 721 **ARS: Aerosol Remote Sensing**
- 722 **BG test: Breusch-Godfrey test**
- 723 **CAL: Continuous Aerosol Layer**
- 724 **CAMAERA: CAMs AERosol Advancement**
- 725 **CAMS: Copernicus Atmosphere Monitoring Service**
- 726 **CHM15k: Lufft automated lidar-ceilometer instrument**
- 727 **CL61: Vaisala polarisation sensitive lidar-ceilometer instrument**
- 728 **CNR-ISAC: National Research Council - Institute of Atmospheric Sciences and Climate**
- 729 **CWT: Continuous Wavelet Transform**
- 730 **DTW: Dynamic Time Warping**
- 731 **DWD: German Weather Service**
- 732 **EAL: Elevated Aerosol Layer**
- 733 **EARLINET: Aerosol Research Lidar Network**
- 734 **EarthCARE: Cloud, Aerosol and Radiation Explorer**
- 735 **EC: European Community**
- 736 **ECMWF: European Centre for Medium-Range Weather Forecasts**
- 737 **EPA: Environmental Protection Agency**
- 738 **ESA: European Space Agency**
- 739 **ESFRI: European Strategy Forum on Research Infrastructures**
- 740 **E-PROFILE: EUMETNET program coordinating the measurements of wind, aerosol and cloud profiles from radars and**
- 741 **lidars**
- 742 **ERA5: fifth generation ECMWF reanalysis for the global climate and weather**
- 743 **ESFRI: European Strategy Forum on Research Infrastructures**

744 EUMETNET: European Meteorological Services Network
745 IFS: Integrated Forecasting System)
746 INGV: Istituto Nazionale di Geofisica e Vulcanologia
747 JAXA: Japan Aerospace Exploration Agency
748 LR: Lidar Ratio
749 MAL: Mixed Aerosol Layer
750 ML: Mixed Layer
751 MPLnet: Micro-Pulse Lidar Network
752 NASA: National Aeronautics and Space Administration
753 NASA-CALIPSO: NASA-CNES CALIOP sensor onboard CALIPSO
754 OPC: Optical Particle Counter
755 PLC: Polarisation-sensitive automated Lidar-Ceilometer
756 PM: Particulate Matter
757 PROBE: PROFiling the atmospheric Boundary layer at European scale
758 QA: Quality Assurance
759 QC: Quality Control
760 QC.CAL: Quality Control applied within the absolute calibration procedure
761 QC.EAL: Quality Control applied within the ALADIN detection of elevated aerosol layers
762 QC.OVL: Quality Control applied within the overlap correction procedure
763 RI-URBANS: EC H2020 project aimed at developing advanced service tools for air quality monitoring networks
764 RH: Relative Humidity
765 SNR: signal-to-noise ratio
766 SKYNET: ground-based radiation observation network dedicated to aerosol-cloud-solar radiation interaction researches
767 TOPROF: Towards Operational ground based PROFiling with ceilometers, doppler lidars and microwave radiometers
768 VONA: Volcano Observatory Notice for Aviation
769 WHO: World Health Organization

770 **Data availability:** The presented datasets will be made freely accessible and linked to a doi, should the revision process lead
771 to a positive outcome.

772 **Author Contribution:** Conceptualization, Data curation, Investigation: AnB, FB, HD; Formal analysis and Software: AnB;
773 Visualization: AnB, FB, HD; ALC instruments and database management: LDL, AIB, FP, HD, GPG; Funding acquisition
774 and Supervision: FB; Writing – original draft preparation: AnB, FB, HD; Writing – review & editing: AnB, FB, HD, AIB,
775 GPG.

776 **Competing interests:** The authors declare that they have no conflict of interest.

777 **Acknowledgements**

778 This research received partial financial support from the EC H2020 Project RI-URBANS (GA No 101036245), and
779 benefited from work done within the Action PROBE (CA18235), supported by COST (European Cooperation in Science and
780 Technology).

781 A. Bellini performed this work in the framework of her Doctoral Program at University 'La Sapienza' (DIET, Rome, Italy)
782 under the scientific supervision of Dr. Francesca Barnaba and with the financial contribution of RI-URBANS.

783 A. Bracci and F. Pasqualini were supported by the project R0000032 – ITINERIS, Italian Integrated Environmental
784 Research Infrastructures System (D.D. n. 130/2022 - CUP B53C22002150006) Funded by EU - Next Generation EU PNRR-
785 Mission 4 “Education and Research” - Component 2: “From research to business” - Investment 3.1: “Fund for the realisation
786 of an integrated system of research and innovation infrastructures”.

787 We would like to thank: M. Clerico and D. Poggi (PLC-Torino), R. Cresta and A. Bisignano (PLC-Genova), E. Collino and
788 D. Perona (PLC-Milano-Rubattino), C. Cristofanelli (ALC-Mt.Cimone), Samantha Melani and Andrea Antonini (PLC-
789 Firenze), Marco Rosoldi (ALC-Potenza), S. Ottonelli (ALC-Taranto), C.R. Calidonna (ALC-Lamezia Terme), M. Coltelli
790 and R. Gueli (Catania and Etna ALC & PLC systems) for their contribution to the ALICENET infrastructure, and L. Ferrero,
791 A. Di Giosa, M. Furnari and G. Tranchida for support in the ALICENET sites of Milano Bicocca, Rome Downtown,
792 Messina and Capo Granitola, respectively.

793 PLC data in Milan-Rubattino, are collected by RSE in the framework of the 3-Year Research Plan 2022-2024 for the Italian
794 Electrical System (DM MITE n. 337, 15.09.2022), in compliance with the Decree of April 16th, 2018.

795 We acknowledge the Italian Air Force CAMM-Mt.Cimone for their support in the operation of the CMN-IT ceilometer,
796 funded by the Ministry of University and Research (MUR) by the Project "Potenziamento della Rete di Osservazione ICOS-
797 Italia nel Mediterraneo" PRO-ICOS_MED (PIR01_00019), and the GAW-WMO regional station "Rita Atria" for the
798 ceilometer hosting in Capo Granitola.

799 We also gratefully acknowledge S. Gilardoni, P. Bonasoni and A. Provenzale for providing the OPC data collected at the
800 'Testa Grigia' station at Plateau Rosa managed by the CNR Department of Earth System Sciences and Environmental
801 Technologies, and the ARPA Lazio for providing the Rome Tor Vergata TKE dataset.

802 We acknowledge the Copernicus Atmosphere Monitoring Service (CAMS) for the CAMS European air quality forecasts,
803 ENSEMBLE data.

804

805

806

807 **References**

808 Adam, M., Fragkos, K., Biniotoglou, I., Wang, D., Stachlewska, I. S., Belegante, L., and Nicolae, V.: Towards Early
809 Detection of Tropospheric Aerosol Layers Using Monitoring with Ceilometer, Photometer, and Air Mass Trajectories,
810 Remote Sensing, 14(5):1217, <https://doi.org/10.3390/rs14051217>, 2022.

811

812 Andrés Hernández, M. D., Hilboll, A., Ziereis, H., Förster, E., Krüger, O. O., Kaiser, K., Schneider, J., Barnaba, F.,
813 Vrekoussis, M., Schmidt, J., Huntrieser, H., Blechschmidt, A.-M., George, M., Nenakhov, V., Harlass, T., Holanda, B. A.,
814 Wolf, J., Eirenschmalz, L., Krebsbach, M., Pöhlker, M. L., Kalisz Hedegaard, A. B., Mei, L., Pfeilsticker, K., Liu, Y.,
815 Koppmann, R., Schlager, H., Bohn, B., Schumann, U., Richter, A., Schreiner, B., Sauer, D., Baumann, R., Mertens, M.,
816 Jöckel, P., Kilian, M., Stratmann, G., Pöhlker, C., Campanelli, M., Pandolfi, M., Sicard, M., Gómez-Amo, J. L., Pujadas, M.,
817 Bigge, K., Kluge, F., Schwarz, A., Daskalakis, N., Walter, D., Zahn, A., Pöschl, U., Bönisch, H., Borrmann, S., Platt, U., and
818 Burrows, J. P.: Overview: On the transport and transformation of pollutants in the outflow of major population centres –
819 observational data from the EMERGe European intensive operational period in summer 2017, Atmos. Chem. Phys., 22,
820 5877–5924, <https://doi.org/10.5194/acp-22-5877-2022>, 2022.

821

822 Angelini, F., Barnaba, F., Landi, T. C., Caporaso, L., and Gobbi, G. P.: Study of atmospheric aerosols and mixing layer by
823 LIDAR, Radiant. Prot. Dosim., 137, 275–279, <https://doi.org/10.1093/rpd/ncp219>, 2009.

824

825 Ansmann, A., Tesche, M., Seifert, P., Groß, S., Freudenthaler, V., Apituley, A., Wilson, K. M., Serikov, I., Linné, H.,
826 Heinold, B., Hiebsch, A., Schnell, F., Schmidt, J., Mattis, I., Wandinger, U., and Wiegner, M.: Ash and fine-mode particle
827 mass profiles from EARLINET-AERONET observations over central Europe after the eruptions of the Eyjafjallajökull
828 volcano in 2010, J. Geophys. Res., 116, D00U02, doi:10.1029/2010JD015567, 2010.

829

830 Aubinet, M., Grelle, A., Ibrom, A., Rannik, Ü., Moncrieff, J., Foken T., Kowalski, A.S., Martin, P.H., Berbigier, P.,
831 Bernhofer, Ch., Clement, R., Elbers, J., Granier, A., Grünwald, T., Morgenstern, K., Pilegaard, K., Rebmann, C., Snijders,
832 W., Valentini, R., and Vesala, T.: Estimates of the Annual Net Carbon and Water Exchange of Forests: The EUROFLUX
833 Methodology, Advances in Ecological Research, 30, 113-175, [https://doi.org/10.1016/S0065-2504\(08\)60018-5](https://doi.org/10.1016/S0065-2504(08)60018-5), 1999.

834

835 Balestrini, R., Diémoz, H., Freppaz, M., Delconte, C.A., Caschetto, M., Matiatos, I.: Nitrogen atmospheric deposition in a
836 high-altitude Alpine environment: A chemical and isotopic approach to investigate the influence from anthropized areas,
837 Atmos. Environ., 328, 120513, [doi: 10.1016/j.atmosenv.2024.120513](https://doi.org/10.1016/j.atmosenv.2024.120513), 2024.

838

839 Barnaba, F., and Gobbi, G. P.: Lidar estimation of tropospheric aerosol extinction, surface area and volume: Maritime and
840 desert-dust cases, *J. Geophys. Res.*, 106(D3), 3005–3018, doi:10.1029/2000JD900492, 2001.

841

842 Barnaba, F., Putaud, J. P., Gruening, C., Dell’Acqua, A., and Dos Santos, S.: Annual cycle in co-located in situ, total-
843 column,
844 and height-resolved aerosol observations in the Po Valley (Italy): Implications for ground-level particulate matter mass
845 concentration estimation from remote sensing, *J. Geophys. Res.-Atmos.*, 115, D19209,
846 <https://doi.org/10.1029/2009JD013002>, 2010.

847

848 Barnaba, F., Angelini, F., Curci, G., and Gobbi, G. P.: An important fingerprint of wildfires on the European aerosol load,
849 *Atmos. Chem. Phys.*, 11, 10487–10501, <https://doi.org/10.5194/acp-11-10487-2011>, 2011.

850

851 Barnaba, F., Romero, N., Bolignano, A., Basart, S., Renzi, M., and Stafoggia, M.: Multiannual assessment of the desert dust
852 impact on air quality in Italy combining PM10 data with physics-based and geostatistical models, *Environment International*,
853 163, 107204, <https://doi.org/10.1016/j.envint.2022.107204>, 2022.

854

855 Barnaba, F., A. Bellini, H. Diémoz, A. Bracci, L. Di Liberto, F. Pasqualini, L. Mona, J.-C. Dupont, M. Haeffelin, P. Delville,
856 S. Kotthaus, F. Lapouge and C. Pietras, Operational aerosol monitoring through remote sensing in support of air quality
857 networks, *Actris Science Conference*, Rennes, May 13-16, Rennes, France.

858

859 Bedoya-Velásquez, A.E.; Hoyos-Restrepo, M.; Barreto, A.; García, R.D.; Romero-Campos, P.M.; García, O.; Ramos, R.;
860 Roininen, R.; Toledano, C.; Sicard, M.; et al. Estimation of the Mass Concentration of Volcanic Ash Using Ceilometers:
861 Study of Fresh and Transported Plumes from La Palma Volcano. *Remote Sens.* 2022, 14, 5680.
862 <https://doi.org/10.3390/rs14225680>

863

864 Bellini, A., Bracci, A., Diémoz, H., Di Liberto, L., and Barnaba, F.: Multi-annual analysis of aerosol vertical profiles and
865 clouds across Italy derived from the Italian network of Automated Lidar-Ceilometers ALICENET and comparison to
866 relevant Copernicus Atmosphere Monitoring Service (CAMS) data, in preparation, 2024.

867

868 Bonanno, R., Lacavalla, M., and Sperati, S.: A new high resolution Meteorological Reanalysis Italian Dataset: MERIDA, *Q.*
869 *J. Roy. Meteorol. Soc.*, 145, 1756–1779, <https://doi.org/10.1002/qj.3530>, 2019.

870

871 Brenot, H., Theys, N., Clarisse, L., van Gent, J., Hurtmans, D. R., Vandenbussche, S., Papagiannopoulos, N., Mona, L.,
872 Virtanen, T., Uppstu, A., Sofiev, M., Bugliaro, L., Vázquez-Navarro, M., Hedelt, P., Parks, M. M., Barsotti, S., Coltelli, M.,

873 Moreland, W., Scollo, S., Salerno, G., Arnold-Arias, D., Hirtl, M., Peltonen, T., Lahtinen, J., Sievers, K., Lipok, F.,
874 Rüfenacht, R., Haefele, A., Hervo, M., Wagenaar, S., Som de Cerff, W., de Laat, J., Apituley, A., Stammes, P., Laffineur,
875 Q., Delcloo, A., Lennart, R., Rokitansky, C.-H., Vargas, A., Kerschbaum, M., Resch, C., Zopp, R., Plu, M., Peuch, V.-H.,
876 Van Roozendael, M., and Wotawa, G.: EUNADICS-AV early warning system dedicated to supporting aviation in the case of
877 a crisis from natural airborne hazards and radionuclide clouds, *Nat. Hazards Earth Syst. Sci.*, 21, 3367–3405,
878 <https://doi.org/10.5194/nhess-21-3367-2021>, 2021.

879

880 Breusch, T. S.: Testing for Autocorrelation in Dynamic Linear Models, *Australian Economic Papers*, 17, 334–355,
881 [doi:10.1111/j.1467-8454.1978.tb00635.x](https://doi.org/10.1111/j.1467-8454.1978.tb00635.x), 1978.

882

883 Bucci, S., Cristofanelli, P., Decesari, S., Marinoni, A., Sandrini, S., Groß, J., Wiedensohler, A., Di Marco, C. F., Nemitz, E.,
884 Cairo, F., Di Liberto, L., and Fierli, F.: Vertical distribution of aerosol optical properties in the Po Valley during the 2012
885 summer campaigns, *Atmos. Chem. Phys.*, 18, 5371–5389, <https://doi.org/10.5194/acp-18-5371-2018>, 2018.

886

887 Buxmann, J.: Investigating the seasonal fluctuations of the CHM15K Ceilometer calibration constant. Zenodo,
888 <https://zenodo.org/doi/10.5281/zenodo.11108620>, 2024.

889

890 Caicedo, V., Delgado, R., Sakai, R., Knepp, T., Williams, D., Cavender, K., Lefer, B., and Szykman, J.: An Automated
891 Common Algorithm for Planetary Boundary Layer Retrievals Using Aerosol Lidars in Support of the U.S. EPA
892 Photochemical Assessment Monitoring Stations Program, *J. Atmos. Oceanic Technol.*, 37, 1847–1864,
893 <https://doi.org/10.1175/JTECH-D-20-0050.1>, 2020.

894

895 Ceamanos, X., Coopman, Q., George, M., Riedi, J., Parrington, M., and Clerbaux, C.: Remote sensing and model analysis of
896 biomass burning smoke transported across the Atlantic during the 2020 Western US wildfire season, *Sci. Rep.*, 13, 16014,
897 <https://doi.org/10.1038/s41598-023-39312-1>, 2023.

898

899 Chan, K. L., Wiegner, M., Flentje, H., Mattis, I., Wagner, F., Gasteiger, J., and Geiß, A.: Evaluation of ECMWF-IFS
900 (version 41R1) operational model forecasts of aerosol transport by using ceilometer network measurements, *Geosci. Model*
901 *Dev.*, 11, 3807–3831, <https://doi.org/10.5194/gmd-11-3807-2018>, 2018.

902

903 Cimini, D., Haeffelin, M., Kotthaus, S., Löhnert, U., Martinet, P., O’Connor, E., Walden, C., Collaud Coen, M., and
904 Preissler, J.: Towards the profiling of the atmospheric boundary layer at European scale—introducing the COST Action
905 PROBE, *Bull. of Atmos. Sci. & Technol.* 1, 23–42, <https://doi.org/10.1007/s42865-020-00003-8>, 2020.

906

907 Collaud Coen, M., Weingartner, E., Furger, M., Nyeki, S., Prévôt, A. S. H., Steinbacher, M., and Baltensperger, U.: Aerosol
908 climatology and planetary boundary influence at the Jungfraujoch analyzed by synoptic weather types, *Atmos. Chem. Phys.*,
909 11, 5931–5944, <https://doi.org/10.5194/acp-11-5931-2011>, 2011.

910

911 Collaud Coen, M., Andrews, E., Aliaga, D., Andrade, M., Angelov, H., Bukowiecki, N., Ealo, M., Fialho, P., Flentje, H.,
912 Hallar, A. G., Hooda, R., Kalapov, I., Krejci, R., Lin, N.-H., Marinoni, A., Ming, J., Nguyen, N. A., Pandolfi, M., Pont, V.,
913 Ries, L., Rodríguez, S., Schauer, G., Sellegri, K., Sharma, S., Sun, J., Tunved, P., Velasquez, P., and Ruffieux, D.:
914 Identification of topographic features influencing aerosol observations at high altitude stations, *Atmos. Chem. Phys.*, 18,
915 12289–12313, <https://doi.org/10.5194/acp-18-12289-2018>, 2018.

916

917 Córdoba-Jabonero, C., Sicard, M., Ansmann, A., del Águila, A., and Baars, H.: Separation of the optical and mass features
918 of particle components in different aerosol mixtures by using POLIPHON retrievals in synergy with continuous polarized
919 Micro-Pulse Lidar (P-MPL) measurements, *Atmos. Meas. Tech.*, 11, 4775–4795, <https://doi.org/10.5194/amt-11-4775-2018>,
920 2018.

921

922 Corradini, S., Guerrieri, L., Lombardo, V., Merucci, L., Musacchio, M., Prestifilippo, M., Scollo, S., Silvestri, M., Spata, G.,
923 and Stelitano, D.: Proximal monitoring of the 2011-2015 Etna lava fountains using MSG-SEVIRI data. *Geosciences*, 8, 140,
924 <https://doi.org/10.3390/geosciences8040140>, 2018.

925

926 Curci, G., Ferrero, L., Tuccella, P., Barnaba, F., Angelini, F., Bolzacchini, E., Carbone, C., Denier van der Gon, H. A. C.,
927 Facchini, M. C., Gobbi, G. P., Kuenen, J. P. P., Landi, T. C., Perrino, C., Perrone, M. G., Sangiorgi, G., and Stocchi, P.: How
928 much is particulate matter near the ground influenced by upper-level processes within and above the PBL? A summertime
929 case study in Milan (Italy) evidences the distinctive role of nitrate, *Atmos. Chem. Phys.*, 15, 2629–2649,
930 <https://doi.org/10.5194/acp-15-2629-2015>, 2015.

931

932 D'Angelo, L., Rovelli, G., Casati, M., Sangiorgi, G., Perrone, M. G., Bolzacchini, E., and Ferrero, L.: Seasonal behaviour of
933 PM_{2.5} deliquescence, crystallization, and hygroscopic growth in the Po Valley (Milan): Implications for remote sensing
934 applications, *Atmospheric Research*, 176–177, 87-95, <https://doi.org/10.1016/j.atmosres.2016.02.011>, 2016.

935

936 Di Bernardino, A., Iannarelli, A. M., Casadio, S., Perrino, C., Barnaba, F., Tofful, L., Campanelli, M., Di Liberto, L., Mevi,
937 G., Siani, A.M., & Cacciani, M.: Impact of synoptic meteorological conditions on air quality in three different case studies in
938 Rome, Italy. *Atmospheric Pollution Research*, 12(4), 76-88, <https://doi.org/10.1016/j.apr.2021.02.019>, 2021.

939

940 Diémoz, H., Magri, T., Pession, G., Tarricone, C., Tombolato, I.K.F., Fasano, G., and Zublena, M.: Air Quality in the Italian
941 Northwestern Alps during Year 2020: Assessment of the COVID-19 «Lockdown Effect» from Multi-Technique
942 Observations and Models, *Atmosphere*, 12(8):1006, <https://doi.org/10.3390/atmos12081006>, 2021.

943

944 Diémoz, H., Barnaba, F., Magri, T., Pession, G., Dionisi, D., Pittavino, S., Tombolato, I. K. F., Campanelli, M., Della Ceca,
945 L. S., Hervo, M., Di Liberto, L., Ferrero, L., and Gobbi, G. P.: Transport of Po Valley aerosol pollution to the northwestern
946 Alps – Part 1: Phenomenology, *Atmos. Chem. Phys.*, 19, 3065–3095, <https://doi.org/10.5194/acp-19-3065-2019>, 2019.

947

948 Diémoz, H., Gobbi, G. P., Magri, T., Pession, G., Pittavino, S., Tombolato, I. K. F., Campanelli, M., and Barnaba, F.:
949 Transport of Po Valley aerosol pollution to the northwestern Alps – Part 2: Long-term impact on air quality, *Atmos. Chem.*
950 *Phys.*, 19, 10129–10160, <https://doi.org/10.5194/acp-19-10129-2019>, 2019.

951

952 Dionisi, D., Barnaba, F., Diémoz, H., Di Liberto, L., and Gobbi, G. P.: A multiwavelength numerical model in support of
953 quantitative retrievals of aerosol properties from automated lidar ceilometers and test applications for AOT and PM10
954 estimation, *Atmos. Meas. Tech.*, 11, 6013–6042, <https://doi.org/10.5194/amt-11-6013-2018>, 2018.

955

956 Du, P., Kibbe, W. A., and Lin, S. M.: Improved peak detection in mass spectrum by incorporating continuous wavelet
957 transform-based pattern matching, *Bioinformatics*, 22:17, 2059–2065, <https://doi.org/10.1093/bioinformatics/btl355>, 2006.

958

959 Fasano, G., Diémoz, H., Fountoulakis, I., Cassardo, C., Kudo, R., Siani, A. M., and Ferrero, L.: Vertical profile of the clear-
960 sky aerosol direct radiative effect in an Alpine valley, by the synergy of ground-based measurements and radiative transfer
961 simulations, *Bull. of Atmos. Sci. & Technol.*, 2, 11, <https://doi.org/10.1007/s42865-021-00041-w>, 2021.

962

963 Ferrero, L., Riccio, A., Ferrini, B.S., D'Angelo, L., Rovelli, G., Casati, M., Angelini, F., Barnaba, F., Gobbi, G.P., Cataldi,
964 M., Bolzacchini, E.: Satellite AOD conversion into ground PM10, PM2.5 and PM1 over the Po valley (Milan, Italy)
965 exploiting information on aerosol vertical profiles, chemistry, hygroscopicity and meteorology, *Atmospheric Pollution*
966 *Research*, 10:6, 1895-1912, <https://doi.org/10.1016/j.apr.2019.08.003>, 2019.

967

968 Flentje, H., Claude, H., Elste, T., Gilge, S., Köhler, U., Plass-Dülmer, C., Steinbrecht, W., Thomas, W., Werner, A., and
969 Fricke, W.: The Eyjafjallajökull eruption in April 2010 – detection of volcanic plume using in-situ measurements, ozone
970 sondes and lidar-ceilometer profiles, *Atmos. Chem. Phys.*, 10, 10085–10092, <https://doi.org/10.5194/acp-10-10085-2010>,
971 2010.

972

973 Flentje, H., Mattis, I., Kipling, Z., Rémy, S., and Thomas, W.: Evaluation of ECMWF IFS-AER (CAM5) operational
974 forecasts during cycle 41r1–46r1 with calibrated ceilometer profiles over Germany, *Geosci. Model Dev.*, 14, 1721–1751,
975 <https://doi.org/10.5194/gmd-14-1721-2021>, 2021.

976

977 Fountoulakis, I., Papachristopoulou, K., Proestakis, E., Amiridis, V., Kontoes, C., and Kazadzis, S.: Effect of Aerosol
978 Vertical Distribution on the Modeling of Solar Radiation, *Remote Sensing*, 14(5):1143, <https://doi.org/10.3390/rs14051143>,
979 2022.

980

981 Giovannini, L., Ferrero, E., Karl, T., Rotach, M. W., Staquet, C., Trini Castelli, S., and Zardi, D.: Atmospheric Pollutant
982 Dispersion over Complex Terrain: Challenges and Needs for Improving Air Quality Measurements and Modeling,
983 *Atmosphere*, 11(6):646, <https://doi.org/10.3390/atmos11060646>, 2020.

984

985 Gobbi, G.P., Barnaba, F., Di Liberto, L., Bolignano, A., Lucarelli, F., Nava, S., Perrino, C., Pietrodangelo, A., Basart, S.,
986 Costabile, F., Dionisi, D., Rizza, U., Canepari, S., Sozzi, R., Morelli, M., Manigrasso, M., Drewnick, F., Struckmeier, C.,
987 Poenitz, K., and Wille, H.: An inclusive view of Saharan dust advections to Italy and the Central Mediterranean,
988 *Atmospheric Environment*, 201, 242-256, <https://doi.org/10.1016/j.atmosenv.2019.01.002>, 2019.

989

990 Gobb, G.P., Barnaba, F., Blumthaler, M., Labow, G., and Herman, J.R.: Observed effects of particles nonsphericity on the
991 retrieval of marine and desert dust aerosol optical depth by lidar, *Atmospheric Research*, 61:1, 1-14,
992 [https://doi.org/10.1016/S0169-8095\(01\)00104-1](https://doi.org/10.1016/S0169-8095(01)00104-1), 2002.

993

994 Giorgino, T.: Computing and Visualizing Dynamic Time Warping Alignments in R: The dtw Package. *Journal of Statistical*
995 *Software*, 31(7), 1–24, <https://doi.org/10.18637/jss.v031.i07>, 2009.

996

997 Haarig, M., Ansmann, A., Engelmann, R., Baars, H., Toledano, C., Torres, B., Althausen, D., Radenz, M., and Wandinger,
998 U.: First triple-wavelength lidar observations of depolarization and extinction-to-backscatter ratios of Saharan dust, *Atmos.*
999 *Chem. Phys.*, 22, 355–369, <https://doi.org/10.5194/acp-22-355-2022>, 2022.

1000

1001 Haeffelin, M., Angelini, F., Morille, Y., Martucci, G., Frey, S., Gobbi, G. P., Lolli, S., O’Dowd, C. D., Sauvage, L., Xueref-
1002 Rémy, I., Wastine, B., and Feist D. G.: Evaluation of Mixing-Height Retrievals from Automatic Profiling Lidars and
1003 Ceilometers in View of Future Integrated Networks in Europe, *Boundary-Layer Meteorol.*, 143, 49–75,
1004 <https://doi.org/10.1007/s10546-011-9643-z>, 2012.

1005

1006 Haeffelin, M., Laffineur, Q., Bravo-Aranda, J.-A., Drouin, M.-A., Casquero-Vera, J.-A., Dupont, J.-C., and De Backer, H.:
1007 Radiation fog formation alerts using attenuated backscatter power from automatic lidars and ceilometers, *Atmos. Meas.*
1008 *Tech.*, 9, 5347–5365, <https://doi.org/10.5194/amt-9-5347-2016>, 2016.

1009

1010 Hervo, M., Poltera, Y., and Haefele, A.: An empirical method to correct for temperature-dependent variations in the overlap
1011 function of CHM15k ceilometers, *Atmos. Meas. Tech.*, 9, 2947–2959, <https://doi.org/10.5194/amt-9-2947-2016>, 2016.

1012

1013 Illingworth, A.J., Barker, H.W., Beljaars, A., Ceccaldi, M., Chepfer, H., Clerbaux, N., Cole, J., Delanoë, J., Domenech, C.,
1014 Donovan, D.P., Fukuda, S., Hidakata, M., Hogan, R. J., Huenerbein, A., Kollias, P., Kubota T., Nakajima, T., Nakajima, T.
1015 Y., Nishizawa, T., Ohno, Y., Okamoto, H., Oki, R., Sato, K., Satoh, M., Shephard, M. W., Velázquez-Blázquez, A.,
1016 Wandinger, U., Wehr, T., and van Zadelhoff, G. J.: The EarthCARE satellite: The next step forward in global measurements
1017 of clouds, aerosols, precipitation, and radiation. *Bull. Am. Meteorol. Soc.*, 96, 1311–1332, 10.1175/BAMS-D-12-00227.1,
1018 2015.

1019

1020 Jänicke, L.K., Preusker, R., Docter, N., Fischer, J.: Estimation of Aerosol Layer Height from OLCI Measurements in the
1021 O2A-Absorption Band over Oceans, *Remote Sensing*, 15(16):4080. <https://doi.org/10.3390/rs15164080>, 2023.

1022

1023 Jozef, G. C., Cassano, J. J., Dahlke, S., Dice, M., Cox, C. J., and de Boer, G.: An overview of the vertical structure of the
1024 atmospheric boundary layer in the central Arctic during MOSAiC, *Atmos. Chem. Phys.*, 24, 1429–1450,
1025 <https://doi.org/10.5194/acp-24-1429-2024>, 2024.

1026

1027 IPCC, 2022: *Climate Change 2022: Impacts, Adaptation, and Vulnerability. Contribution of Working Group II to the Sixth*
1028 *Assessment Report of the Intergovernmental Panel on Climate Change*, Cambridge University Press, 3056,
1029 doi:10.1017/9781009325844, 2022.

1030

1031 Körmöndi, B., Szkordilisz, F., Kotthaus, S., Haeffelin, M., Céspedes, J., Martinet, P., Jurcakova, K., Bellini, A., Diémoz, H.,
1032 & Barnaba, F. (2024). Impact of atmospheric boundary layer profiling: Urban environments (D1.5). Zenodo.
1033 <https://doi.org/10.5281/zenodo.11584507>

1034

1035 Kotthaus, S., Haeffelin, M., Drouin, M.-A., Dupont, J.-C., Grimmond, S., Haefele, A., Hervo, M., Poltera, Y., Wiegner, M.:
1036 Tailored Algorithms for the Detection of the Atmospheric Boundary Layer Height from Common Automatic Lidars and
1037 Ceilometers (ALC), *Remote Sensing*, 12(19):3259, <https://doi.org/10.3390/rs12193259>, 2020.

1038

1039 Kotthaus, S., Bravo-Aranda, J. A., Collaud Coen, M., Guerrero-Rascado, J. L., Costa, M. J., Cimini, D., O'Connor, E. J.,
1040 Hervo, M., Alados-Arboledas, L., Jiménez-Portaz, M., Mona, L., Ruffieux, D., Illingworth, A., and Haeffelin, M.:
1041 Atmospheric boundary layer height from ground-based remote sensing: a review of capabilities and limitations, *Atmos.*
1042 *Meas. Tech.*, 16, 433–479, <https://doi.org/10.5194/amt-16-433-2023>, 2023.

1043

1044 Kotthaus, S., Bravo Aranda, J. A.: Deliverable 2.1 Advanced ABL profiling: ABL characterisation, Zenodo,
1045 <https://doi.org/10.5281/zenodo.11636591>, 2024.

1046

1047 Klett J. D.: Lidar inversion with variable backscatter/extinction ratios, *Appl. Opt.* 24, 1638-1643,
1048 <https://doi.org/10.1364/AO.24.001638>, 1985.

1049

1050 Michalsky, J.: The Astronomical Almanac's algorithm for approximate solar position (1950–2050), *Solar Energy*, 40(3),
1051 227-235, [https://doi.org/10.1016/0038-092X\(88\)90045-X](https://doi.org/10.1016/0038-092X(88)90045-X), 1988.

1052

1053 Mira-Salama, D., Van Dingenen, R., Gruening, C., Putaud, J.-P., Cavalli, F., Cavalli, P., Erdmann, N., Dell'Acqua, A., Dos
1054 Santos, S., Hjorth, J., Raes, F., and Jensen, N. R.: Using Föhn conditions to characterize urban and regional sources of
1055 particles, *Atmos. Res.*, 90, 159–169, 2008.

1056

1057 Monteiro, A., Basart, S., Kazadzis, S., Votsis, A., Gkikas, A., Vandenbussche, S., Tobias, A., Gama, C., Pérez García-Pando,
1058 C., Terradellas, E., Notas, G., Middleton, K., Kushta, J., Amiridis, V., Lagouvardos, K., Kosmopoulos, P., Kotroni, V.,
1059 Kanakidou, M., Mihalopoulos, N., Kalivitis, N., Dagsson-Waldhauserová, P., El-Askary, H., Sievers, K., Giannaros, T.,
1060 Mona, L., Hirtl, M., Skomorowski, P., Virtanen, T., Christoudias, T., Di Mauro, B., Trippetta, S., Kutuzov, S., Meinander,
1061 O., and Nickovic, S.: Multi-sectoral impact assessment of an extreme African dust episode in the Eastern Mediterranean in
1062 March 2018, *Science of The Total Environment*, 843, <https://doi.org/10.1016/j.scitotenv.2022.156861>, 2022.

1063

1064 Moreira et al., 2019 <https://doi.org/10.1016/j.atmosres.2020.104932>

1065

1066 Morille, Y., Haeffelin, M., Drobinski, P., and Pelon J.: STRAT: An Automated Algorithm to Retrieve the Vertical Structure
1067 of the Atmosphere from Single-Channel Lidar Data, *J. Atmos. Oceanic Technol.*, 24, 761–775,
1068 <https://doi.org/10.1175/JTECH2008.1>, 2007.

1069

1070 Mortier, A., Goloub, P., Podvin, T., Deroo, C., Chaikovsky, A., Ajtai, N., Blarel, L., Tanre, D., and Derimian, Y.: Detection
1071 and characterization of volcanic ash plumes over Lille during the Eyjafjallajökull eruption, *Atmos. Chem. Phys.*, 13, 3705–
1072 3720, <https://doi.org/10.5194/acp-13-3705-2013>, 2013.

1073

1074 Napoli, A., Desbiolles, F., Parodi, A., and Pasquero, C.: Aerosol indirect effects in complex-orography areas: a numerical
1075 study over the Great Alpine Region, *Atmos. Chem. Phys.*, 22, 3901–3909, <https://doi.org/10.5194/acp-22-3901-2022>, 2022.

1076

1077 Nicolae, D., Vasilescu, J., Talianu, C., Biniotoglou, I., Nicolae, V., Andrei, S., and Antonescu, B.: A neural network aerosol-
1078 typing algorithm based on lidar data, *Atmos. Chem. Phys.*, 18, 14511–14537, <https://doi.org/10.5194/acp-18-14511-2018>,
1079 2018.

1080

1081 Omar, A. H., Winker D. M., Vaughan, M. A., Hu, Y., Treppe, C. R., Ferrare, R. A., Lee K. P., Hostetler, C., Kittaka, C.,
1082 Rogers, R. R., Kuehn R. E., and Liu, Z.: The CALIPSO Automated Aerosol Classification and Lidar Ratio Selection
1083 Algorithm, *J. Atmos. Oceanic Technol.*, 26, 1994–2014, <https://doi.org/10.1175/2009JTECHA1231.1>, 2009.

1084

1085 Osborne, M., Malavelle, F. F., Adam, M., Buxmann, J., Sugier, J., Marengo, F., and Haywood, J.: Saharan dust and biomass
1086 burning aerosols during ex-hurricane Ophelia: observations from the new UK lidar and sun-photometer network, *Atmos.*
1087 *Chem. Phys.*, 19, 3557–3578, <https://doi.org/10.5194/acp-19-3557-2019>, 2019.

1088

1089 Osborne, M. J., de Leeuw, J., Witham, C., Schmidt, A., Beckett, F., Kristiansen, N., Buxmann, J., Saint, C., Welton, E. J.,
1090 Fochesatto, J., Gomes, A. R., Bundke, U., Petzold, A., Marengo, F., and Haywood, J.: The 2019 Raikoke volcanic eruption –
1091 Part 2: Particle-phase dispersion and concurrent wildfire smoke emissions, *Atmos. Chem. Phys.*, 22, 2975–2997,
1092 <https://doi.org/10.5194/acp-22-2975-2022>, 2022.

1093

1094 Osborne, M. J.: Comparison of CHM15k extinction and mass products from ALICE net, A-Profiles and the UK Met Office,
1095 Zenodo, <https://doi.org/10.5281/zenodo.11196654>, 2024.

1096

1097 Papachristopoulou, K., Fountoulakis, I., Bais, A. F., Psiloglou, B. E., Papadimitriou, N., Raptis, I.-P., Kazantzidis, A.,
1098 Kontoes, C., Hatzaki, M., and Kazadzis, S.: Effects of clouds and aerosols on downwelling surface solar irradiance
1099 nowcasting and short-term forecasting, *Atmos. Meas. Tech. Discuss.*, <https://doi.org/10.5194/amt-2023-110>, accepted for
1100 publication 2024.

1101

1102 Papagiannopoulos, N., D'Amico, G., Gialitaki, A., Ajtai, N., Alados-Arboledas, L., Amodeo, A., Amiridis, V., Baars, H.,
1103 Balis, D., Biniotoglou, I., Comerón, A., Dionisi, D., Falconieri, A., Fréville, P., Kampouri, A., Mattis, I., Mijić, Z., Molero,
1104 F., Papayannis, A., Pappalardo, G., Rodríguez-Gómez, A., Solomos, S., and Mona, L.: An EARLINET early warning system
1105 for atmospheric aerosol aviation hazards, *Atmos. Chem. Phys.*, 20, 10775–10789, [https://doi.org/10.5194/acp-20-10775-](https://doi.org/10.5194/acp-20-10775-2020)
1106 2020, 2020.

1107

1108 Poltera, Y., Martucci, G., Collaud Coen, M., Hervo, M., Emmenegger, L., Henne, S., Brunner, D., and Haeefele, A.:
1109 PathfinderTURB: an automatic boundary layer algorithm. Development, validation and application to study the impact on in
1110 situ measurements at the Jungfraujoch, *Atmos. Chem. Phys.*, 17, 10051–10070, <https://doi.org/10.5194/acp-17-10051-2017>,
1111 2017.

1112

1113 Ravnik, L., Laffineur, Q., Ferrario, M. E., Diémoz, H., & Kotthaus, S. (2024). Impact of atmospheric boundary layer
1114 profiling for Environmental agencies and air quality. Zenodo. <https://doi.org/10.5281/zenodo.11176517>

1115

1116 Remer, L. A., Levy, R. C., and Martins, J. V.: Opinion: Aerosol remote sensing over the next 20 years, *Atmos. Chem. Phys.*,
1117 24, 2113–2127, <https://doi.org/10.5194/acp-24-2113-2024>, 2024.

1118

1119 Rizza, U., Barnaba, F., Miglietta, M. M., Mangia, C., Di Liberto, L., Dionisi, D., Costabile, F., Grasso, F., and Gobbi, G. P.:
1120 WRF-Chem model simulations of a dust outbreak over the central Mediterranean and comparison with multi-sensor desert
1121 dust observations, *Atmos. Chem. Phys.*, 17, 93–115, <https://doi.org/10.5194/acp-17-93-2017>, 2017.

1122

1123 Rizza, U., Avolio, E., Morichetti, M., Di Liberto, L., Bellini, A., Barnaba, F., Virgili, S., Passerini, G., and Mancinelli, E.:
1124 On the Interplay between Desert Dust and Meteorology Based on WRF-Chem Simulations and Remote Sensing
1125 Observations in the Mediterranean Basin, *Remote Sensing*, 15(2):435, <https://doi.org/10.3390/rs15020435>, 2023.

1126

1127 Rodríguez, S., Querol, X., Alastuey, A., Kallos, G, and Kakaliagou, O.: Saharan dust contributions to PM10 and TSP levels
1128 in Southern and Eastern Spain, *Atmospheric Environment*, 35(24), 33-2447, [https://doi.org/10.1016/S1352-2310\(00\)00496-](https://doi.org/10.1016/S1352-2310(00)00496-9)
1129 [9](https://doi.org/10.1016/S1352-2310(00)00496-9), 2001.

1130

1131 Ryder, C. L., Bézier, C., Dacre, H. F., Clarkson, R., Amiridis, V., Marinou, E., Proestakis, E., Kipling, Z., Benedetti, A.,
1132 Parrington, M., Rémy, S., and Vaughan, M.: Aircraft engine dust ingestion at global airports, *Nat. Hazards Earth Syst. Sci.*,
1133 24, 2263–2284, <https://doi.org/10.5194/nhess-24-2263-2024>, 2024.

1134

1135 Salgueiro et al., 2023 <https://doi.org/10.1016/j.rse.2023.113684>

1136

1137 Sandrini, S., van Pinxteren, D., Giulianelli, L., Herrmann, H., Poulain, L., Facchini, M. C., Gilardoni, S., Rinaldi, M.,
1138 Paglione, M., Turpin, B. J., Pollini, F., Bucci, S., Zanca, N., and Decesari, S.: Size-resolved aerosol composition at an urban
1139 and a rural site in the Po Valley in summertime: implications for secondary aerosol formation, *Atmos. Chem. Phys.*, 16,
1140 10879–10897, <https://doi.org/10.5194/acp-16-10879-2016>, 2016.

91
92

1141
1142 Scollo, S., Prestifilippo, M., Bonadonna, C., Cioni, R., Corradini, S., Degruyter, W., Rossi, E., Silvestri, M., Biale, E.,
1143 Carparelli, G., Cassisi, C., Merucci, L., Musacchio, M., and Pecora, E.: Near-Real-Time Tephra Fallout Assessment at Mt.
1144 Etna, Italy, *Remote Sensing*, 11(24):2987, <https://doi.org/10.3390/rs11242987>, 2019.

1145
1146 Serafin, S., Adler, B., Cuxart, J., De Wekker, S.F.J., Gohm, A., Grisogono, B., Kalthoff, N., Kirshbaum, D.J., Rotach, M.W.,
1147 Schmidli, J., Stiperski, I., Večenaj, Z., and Zardi, D.: Exchange Processes in the Atmospheric Boundary Layer Over
1148 Mountainous Terrain. *Atmosphere*. 2018; 9(3):102. <https://doi.org/10.3390/atmos9030102>, 2018.

1149
1150 Shang, X., Lipponen, A., Filioglou, M., Sundström, A.-M., Parrington, M., Buchard, V., Darmenov, A. S., Welton, E. J.,
1151 Marinou, E., Amiridis, V., Sicard, M., Rodríguez-Gómez, A., Komppula, M., and Mielonen, T.: Monitoring biomass burning
1152 aerosol transport using CALIOP observations and reanalysis models: a Canadian wildfire event in 2019, *Atmos. Chem.*
1153 *Phys.*, 24, 1329–1344, <https://doi.org/10.5194/acp-24-1329-2024>, 2024.

1154
1155 Shang, X., Mielonen, T., Lipponen, A., Giannakaki, E., Leskinen, A., Buchard, V., Darmenov, A. S., Kukkurainen, A.,
1156 Arola, A., O'Connor, E., Hirsikko, A., and Komppula, M.: Mass concentration estimates of long-range-transported Canadian
1157 biomass burning aerosols from a multi-wavelength Raman polarisation lidar and a ceilometer in Finland, *Atmos. Meas.*
1158 *Tech.*, 14, 6159–6179, <https://doi.org/10.5194/amt-14-6159-2021>, 2021.

1159
1160 Shimizu, A., Nishizawa, T., Jin, Y., Kim, S.-W., Wang, Z., Batdorj, D., and Sugimoto, N.: Evolution of a lidar network for
1161 tropospheric aerosol detection in East Asia, *SPIE. Optical Engineering*, 56, 1–12, <https://doi.org/10.1117/1.OE.56.3.031219>,
1162 2016.

1163
1164 Speidel, J. and Vogelmann, H.: Correct(ed) Klett–Fernald algorithm for elastic aerosol backscatter retrievals: a sensitivity
1165 analysis, *Appl. Opt.* 62, 861-868, <https://doi.org/10.1364/AO.465944>, 2023.

1166
1167 Tesche, M., Ansmann, A., Müller, D., Althausen, D., Engelmann, R., Freudenthaler, V., and Groß, S.: Vertically resolved
1168 separation of dust and smoke over Cape Verde using multiwavelength Raman and polarisation lidars during Saharan Mineral
1169 Dust Experiment 2008, *J. Geophys. Res.*, 114, D13202, doi:10.1029/2009JD011862, 2009.

1170
1171 Tositti, L., Brattich, E., Cassardo, C., Morozzi, P., Bracci, A., Marinoni, A., Di Sabatino, S., Porcù, F., and Zappi, A.:
1172 Development and evolution of an anomalous Asian dust event across Europe in March 2020, *Atmos. Chem. Phys.*, 22, 4047–
1173 4073, <https://doi.org/10.5194/acp-22-4047-2022>, 2022.

1174

1175 Uchiyama, A., Matsunaga, T., and Yamazaki, A.: The instrument constant of sky radiometers (POM-02) – Part 2: Solid view
1176 angle, *Atmos. Meas. Tech.*, 11, 5389–5402, <https://doi.org/10.5194/amt-11-5389-2018>, 2018.
1177

1178 Van Hove, M., Diémoz, H.: Seasonal variation in the Rayleigh calibration factor of Automatic Lidar- Ceilometers: amplitude
1179 across Europe and possible explanations. Zenodo, <https://doi.org/10.5281/zenodo.11074353>, 2024.
1180

1181 Van Tricht, K., Gorodetskaya, I. V., Lhermitte, S., Turner, D. D., Schween, J. H., and Van Lipzig, N. P. M.: An improved
1182 algorithm for polar cloud-base detection by ceilometer over the ice sheets, *Atmos. Meas. Tech.*, 7, 1153–1167,
1183 <https://doi.org/10.5194/amt-7-1153-2014>, 2014.
1184

1185 van Zadelhoff, G.-J., Donovan, D. P., and Wang, P.: Detection of aerosol and cloud features for the EarthCARE atmospheric
1186 lidar (ATLID): the ATLID FeatureMask (A-FM) product, *Atmos. Meas. Tech.*, 16, 3631–3651, <https://doi.org/10.5194/amt-16-3631-2023>, 2023.
1187
1188

1189 Vivone, G., D'Amico, G., Summa, D., Lolli, S., Amodeo, A., Bortoli, D., and Pappalardo, G.: Atmospheric boundary layer
1190 height estimation from aerosol lidar: a new approach based on morphological image processing techniques, *Atmos. Chem.
1191 Phys.*, 21, 4249–4265, <https://doi.org/10.5194/acp-21-4249-2021>, 2021
1192

1193 Wiegner, M. and Gasteiger, J.: Correction of water vapour absorption for aerosol remote sensing with ceilometers, *Atmos.
1194 Meas. Tech.*, 8, 3971–3984, <https://doi.org/10.5194/amt-8-3971-2015>, 2015.
1195

1196 Wiegner, M. and Geiß, A.: Aerosol profiling with the Jenoptik ceilometer CHM15kx, *Atmos. Meas. Tech.*, 5, 1953–1964,
1197 <https://doi.org/10.5194/amt-5-1953-2012>, 2012.
1198

1199 Wiegner, M., Madonna, F., Binietoglou, I., Forkel, R., Gasteiger, J., Geiß, A., Pappalardo, G., Schäfer, K., and Thomas, W.:
1200 What is the benefit of ceilometers for aerosol remote sensing? An answer from EARLINET, *Atmos. Meas. Tech.*, 7, 1979–
1201 1997, <https://doi.org/10.5194/amt-7-1979-2014>, 2014.
1202

1203 Winker, D.M., Pelon, J., Coakley, J.A., Ackerman, S.A., Charlson, R.J., Colarco, P.R., Flamant, P., Fu, Q., Hoff, R.M.,
1204 Kittaka, C., : The CALIPSO mission: A global 3D view of aerosols and clouds. *Bull. Am. Meteorol. Soc.*, 91, 1211–1230,
1205 <https://doi.org/10.1175/2010BAMS3009.1>, 2010.
1206

1207 Welton, E.J., Campbell, J. R., Spinhirne, J. D., and Scott, V. S.: Global monitoring of clouds and aerosols using a network of
1208 micro-pulse lidar systems, *Proc. SPIE*, 4153, 151-158, 10.1117/12.417040, 2000.

1209

1210 Welton, E. J., Stewart, S. A., Lewis, J. R., Belcher, L. R., Campbell, J. R., and Lolli, S.: Status of the NASA Micro Pulse
1211 Lidar Network (MPLNET): overview of the network and future plans, new version 3 data products, and the polarised MPL,
1212 EPJ Web Conf., 176, 09003, <https://doi.org/10.1051/EPJCONF/201817609003>, 2018.

1213

1214 WHO, 2021: WHO global air quality guidelines: particulate matter (PM_{2.5} and PM₁₀), ozone, nitrogen dioxide, sulphur
1215 dioxide and carbon monoxide, Licence: CC BY-NC-SA 3.0 IGO, <https://iris.who.int/handle/10665/345329> , 2021.